Interplay of two E_g orbitals in superconducting $La_3Ni_2O_7$ under pressure

Chen Lu [1,*] Zhiming Pan,[2,1,*] Fan Yang,[3,†] and Congjun Wu [1,2,4,5,‡]

[1]*New Cornerstone Science Laboratory, Department of Physics, School of Science, Westlake University, Hangzhou 310024, Zhejiang, China*

[2]*Institute for Theoretical Sciences, Westlake University, Hangzhou 310024, Zhejiang, China*

[3]*School of Physics, Beijing Institute of Technology, Beijing 100081, China*

[4]*Key Laboratory for Quantum Materials of Zhejiang Province, School of Science, Westlake University, Hangzhou 310024, Zhejiang, China*

[5]*Institute of Natural Sciences, Westlake Institute for Advanced Study, Hangzhou 310024, Zhejiang, China*

(Received 10 December 2023; revised 7 July 2024; accepted 26 August 2024; published 16 September 2024)

The discovery of high-T_c superconductivity (SC) in $La_3Ni_2O_7$ (LNO) has aroused a great deal of interest. Previously, it was proposed that the Ni-$3d_{z^2}$ orbital is crucial to realize the high-T_c SC in LNO. The preformed Cooper pairs therein acquire coherence via hybridization with the $3d_{x^2-y^2}$ orbital to form the SC. However, we held a different viewpoint that the interlayer pairing s-wave SC is induced by the $3d_{x^2-y^2}$ orbital, driven by the strong interlayer superexchange interaction. To include effects from both E_g orbitals, we establish a two-orbital bilayer t-J model. Our calculations reveal that due to the no-double-occupancy constraint, the $3d_{x^2-y^2}$ band and the $3d_{z^2}$ bonding band are flattened by a factor of about 2 and 10, respectively, which is consistent with recent angle-resolved photoemission spectroscopy measurements. Consequently, a high-temperature SC can be hardly induced in the $3d_{z^2}$ orbital due to the difficulty to develop phase coherence. However, it can be easily achieved by the $3d_{x^2-y^2}$ orbital under realistic interaction strength. With electron doping, the $3d_{z^2}$-band gradually dives below the Fermi level, but T_c continues to enhance, suggesting that it is not necessary for the high-T_c SC in LNO. With hole doping, T_c initially drops and then rises, accompanied by the crossover from the BCS to BEC-type superconducting transitions.

DOI: 10.1103/PhysRevB.110.094509

I. INTRODUCTION

The recent discovery of high-temperature ($T_c \approx 80$ K) superconductivity (SC) in $La_3Ni_2O_7$ (LNO) under pressures over 14 GPa [1] has aroused intensive interests, both experimental [2–11] and theoretical [12–61]. LNO and its possible generalizations $R_3Ni_2O_7$ (R=rare-earth element) [32,41,44] serve as a newly platform for high-T_c SC other than the cuprates [62]. Although LNO hosts the conducting NiO_2 plane isostructural with the CuO_2 plane in cuprates, two significant differences exist between these two families in the aspect of crystal and electronic structures.

Firstly, in multilayered cuprates, the electronic properties and spin exchanges primarily stem from the Cu-$3d_{x^2-y^2}$ and O-$2p$ orbitals within the CuO_2 plane, leading to robust intralayer pairing. The interlayer hopping within each unit cell is weak [63–71], resulting in interlayer Copper pair tunneling [72–74]. In stark contrast, the LNO compound possesses two NiO_2 layers within a unit cell, strongly intertwined via the $3d_{z^2}$ orbital. This robust hybridization is facilitated by the Ni-O-Ni bonding, further assisted by the O-$2p$ orbitals of the apical oxygen atoms. Note that although LNO is an existing material studied previously [75–92], its properties undergo a fundamental change due to the structure transition from the orthorhombic structure with space group *Amam* [92] to *Fmmm* under pressure. The Ni-O-Ni bonding angle changes from 168° to 180° enhancing the interlayer hybridization, after which high-T_c SC emerges. This fact implies the crucial importance of the interlayer coupling for the emergence of high-T_c SC in the pressurized LNO. Studies on bilayer Hubbard models exist in literature [93–97]. In particular, an extended version of bilayer Hubbard model shows high-T_c superconductivity arising from doping antiferromagnetic Mott insulators by sign-problem free quantum Monte Carlo (QMC) simulations, nevertheless, a strong interlayer antiferromagnetic superexchange is required [97].

Secondly, while cuprate can essentially be treated as a single orbital system, the LNO with $Ni^{2.5+}$ electron configuration simultaneously hosts two low-energy E_g orbitals, i.e., the nearly half-filled $3d_{z^2}$ orbital and the nearly quarter-filled $3d_{x^2-y^2}$ orbital [1,5,12,13,86,87]. Both orbitals are important in LNO: while the $3d_{z^2}$ orbital connects two NiO_2 layers via the Ni-O-Ni bonding, the $3d_{x^2-y^2}$ orbital is responsible for the intralayer transport. At a glance, knowledge from cuprates [98–100] seems to suggest that neither the half-filling nor the quarter-filling can provide an ideal platform to realize high-T_c SC. However, the situations might be dramatically changed when the interplay between the two E_g orbitals and the bilayer structure are taken into account. On the one hand, there exists the nearest-neighbor (NN) bond hybridization between the two E_g orbitals, which dictates that the concentrate of charge

*These authors contributed equally to this work.
†Contact author: yangfan_blg@bit.edu.cn
‡Contact author: wucongjun@westlake.edu.cn

carrier is transformed between two orbitals. On the other hand, Hund's rule coupling polarizes electrons in two orbitals on the same site, which induces considerable interlayer antiferromagnetic exchange between $3d_{x^2-y^2}$ orbitals intermediated with the d_{z^2} orbitals [25].

There are often two different viewpoints on the strong-coupling analysis to the high-T_c SC in the pressurized LNO: Which orbital plays the primary role? One viewpoint is that the $3d_{z^2}$ orbital dominates [22,30,34]. Since its orbital orientation is along the z axis, the interlayer antiferromagnetic (AFM) superexchange between $3d_{z^2}$ orbitals is large. Two electrons in the $3d_{z^2}$ orbital along the rung in a unit cell already pair below a high-temperature scale T^*. However, these pairs still need to hop in the NiO_2 planes to develop phase coherence. Two difficulties arises in this regard: one is the low hole density of the $3d_{z^2}$ orbital, and the other is the weak intralayer hopping integral between the adjacent $3d_{z^2}$ orbitals. It was proposed [1,18] that pressure could enhance the hybridization between two E_g orbitals and lift up the σ-bonding band consisting of the $3d_{z^2}$ orbital to cross the Fermi level, i.e., to metallize, which could settle both difficulties, paving way for the $3d_{z^2}$ orbital to take the dominant role in the SC.

In contrast, the other viewpoint emphasized on the $3d_{x^2-y^2}$ orbital [25,27,29]. The key observation is the Hund's rule coupling between two E_g orbitals on the same Ni site. Integrating out the nearly localized spin moment of the $3d_{z^2}$ orbital under the strong Hund's rule coupling, an effective strong interlayer superexchange between the $3d_{x^2-y^2}$ orbitals is generated. Therefore an effective bilayer single-$3d_{x^2-y^2}$ orbital t-$J_\parallel$-$J_\perp$ model is obtained [25]. In addition to the conventional intralayer superexchange $J_\parallel$, two layers are coupled by the strong interlayer superexchange $J_\perp$. $J_\perp$ favors an interlayer s-pairing SC and enhances the T_c dramatically [25,97]. In this point of view, the role of pressure lies in that it changes the lattice structure and therefore significantly enhances the interlayer superexchange.

In this work, in order to study both E_g orbitals on equal footing, we establish an effective two-orbital bilayer t-J model to study their interplay, treated by the slave-boson mean-field (SBMF) analysis [98,101]. In the strong coupling limit with a large Hubbard U, double occupied state for each orbital is energetically unfavorable, leading to its effective projection out of the Hilbert space. The first result is that due to this no-double-occupancy constraint, the $3d_{x^2-y^2}$ band and the σ-bonding $3d_{z^2}$ band are flattened by a factor of about 2 and 10, respectively, which is well consistent with the recent angular resolved photo emission spectroscopy (ARPES) measurement [5]. The second result is that the interlayer s-wave SC in LNO is induced by the pairing of the $3d_{x^2-y^2}$ orbital. For the $3d_{z^2}$ orbital, as the no-double-occupancy constraint strongly suppresses its hybridization with the $3d_{x^2-y^2}$ orbital, it can hardly acquire sufficient coherence to account for the high $T_c \approx 80$ K comparable with experiment, which however is tenable for the $3d_{x^2-y^2}$ orbital under realistic interaction parameters. The final result is the doping versus temperature phase diagram. With the electron doping the T_c monotonically increases although the σ-bonding band gradually dives below the Fermi level, suggesting that the metallization of the bonding band is not necessary for the high-T_c SC in LNO. With the hole doping the T_c initially decreases and then increases, and the superconducting transition is initially the BCS type and then crossover to the BEC type. Above T_c, there exists a pseudogap phase characterized by the pairing of the $3d_{z^2}$ spinons, which merges into the superconducting phase after some critical electron doping level. Such an interesting phase diagram with coexisting T_c and T^* appeals for experimental verification in the near future.

The rest part of this paper is organized as follow. In Sec. II, the effective bilayer two-orbital model for LNO is established. In Sec. III, we introduce the SBMF approach to treat the two-orbital model, and the band renormalization effect is further revealed by the electron correlation. In Sec. IV, the SC state of the two-orbital model is studied. We shall first study the SC induced by the two orbitals separately and then clarify the obtained SC in the combined system. In Sec. V, the effect of possible chemical doping in LNO is explored and the phase diagram including the pseudogap phase is obtained. The conclusion is presented in Sec. VII.

II. EFFECTIVE BILAYER TWO-ORBITAL MODEL

The electronic properties of the LNO material are determined by the E_g orbitals of two $Ni^{2.5+}$ cations along the rung connecting the NiO_2 bilayer planes, whose energy bands are close to the Fermi energy. Below the bilayer two-orbital model are constructed to describe the band structure and super-exchange physics.

A. The bilayer two-orbital Hubbard Hamiltonian

The different orientations of two E_g orbitals result in the strong interlayer hopping $t_\perp^z$ between two $3d_{z^2}$ orbitals along the rung, and also the relatively strong intralayer hopping $t_\parallel^x$ between the $3d_{x^2-y^2}$ orbitals. The $3d_{z^2}$ and $3d_{x^2-y^2}$ orbitals within the intralayer nearest neighbor (NN) bond further hybridize, but those along the rung do not. The corresponding band structure is formulated in the following tight-binding Hamiltonian:

$$\begin{aligned} H_0 = & -t_\parallel^x \sum_{\langle i,j\rangle\alpha\sigma} \left(d^\dagger_{x^2\alpha\sigma}(i) d_{x^2\alpha\sigma}(j) + \text{H.c.}\right) + \Delta_g \sum_{i\alpha\sigma} d^\dagger_{x^2\alpha\sigma}(i) d_{x^2\alpha\sigma}(i) \\ & - t_\perp^z \sum_{i\sigma} \left(d^\dagger_{z^2 1\sigma}(i) d_{z^2 2\sigma}(i) + \text{H.c.}\right) - t_\parallel^z \sum_{\langle i,j\rangle\alpha\sigma} \left(d^\dagger_{z^2\alpha\sigma}(i) d_{z^2\alpha\sigma}(j) + \text{H.c.}\right) - \sum_{\langle i,j\rangle\alpha\sigma} t^{xz}_{\parallel,j-i} \left(d^\dagger_{x^2\alpha\sigma}(i) d_{z^2\alpha\sigma}(j) + \text{H.c.}\right), \end{aligned} \tag{1}$$

where i is the lattice site index; α represents the layer index; σ is the spin component index. $d^\dagger_{a\alpha\sigma}(i)$ represents the electron creation operator for the $3d_{x^2-y^2}$ orbital ($a = x^2$) or the $3d_{z^2}$ orbital ($a = z^2$) with a referring to the orbital index. The $3d_{z^2}$

orbital has a smaller on-site energy as described by the Δ_g term. The intralayer hybridization $t^{xz}_{\parallel,j-i}$ between $3d_{x^2-y^2}$ and $3d_{z^2}$ orbitals on neighboring sites is comparable to hopping strengths $t^x_\parallel$ and $t^z_\perp$. The NN hybridization takes opposite signs along the x and y direction, respectively, i.e., $t^{xz}_{\parallel,x} = -t^{xz}_{\parallel,y} \equiv t^{xz}_\parallel$, due to the different symmetries of orbital wave functions. A finite but small intralayer hopping $t^z_\parallel$ for the $3d_{z^2}$ orbital is also added into Eq. (1).

The multiorbital Hubbard interaction reads

$$\begin{aligned} H_1 =& U \sum_{ia\alpha} n_{a\alpha\uparrow}(i) n_{a\alpha\downarrow}(i) + V \sum_{i\alpha} n_{z^2\alpha}(i) n_{x^2\alpha}(i) \\ &+ P \sum_{i\alpha} (d^\dagger_{x^2\alpha\uparrow}(i) d^\dagger_{x^2\alpha\downarrow}(i) d_{z^2\alpha\downarrow}(i) d_{z^2\alpha\uparrow}(i) + \text{H.c.}) \\ &- J_H \sum_{i\alpha} \boldsymbol{S}_{z^2\alpha}(i) \cdot \boldsymbol{S}_{x^2\alpha}(i), \end{aligned} \tag{2}$$

where the U and V terms describe the intraorbital and interorbital repulsions, respectively; the P term describes the singlet pair hopping between two orbitals; the J_H term is the Hund's rule coupling aligning electron spins in two onsite E_g orbitals; $n_{a\alpha\sigma}(i) = d^\dagger_{a\alpha\sigma}(i) d_{a\alpha\sigma}(i)$ represents the particle number operator for an electron with spin-σ in orbital a with $a = x^2$ or z^2; $n_{a\alpha}(i) = n_{a\alpha\uparrow}(i) + n_{a\alpha\downarrow}(i)$; $\boldsymbol{S}_{a\alpha}(i) = \frac{1}{2} d^\dagger_{a\alpha}(i)[\boldsymbol{\sigma}] d_{a\alpha}(i)$ is the spin operator for the electron in orbital a, where Pauli matrices $\boldsymbol{\sigma} = (\sigma_x, \sigma_y, \sigma_z)$. Usually, the symmetry condition implies $V = U - J_H$.

We adopt the hopping parameters from the DFT calculation provided by Ref. [32] for the LNO material. The relevant parameters are taken as, $t^x_\parallel = 0.526$ eV, $t^z_\parallel = 0.113$ eV, $t^z_\perp = 0.676$ eV, $t^{xz}_\parallel = 0.25$ eV, and $\Delta_g = 0.528$ eV. The computational results from LDA + U indicate that the Hubbard interaction strength of the system is approximately $U \approx 4.75$ eV [86]. Independent DFT and many-body calculations [12,19,26] reveal that U ranges from 3 to 5 eV. The ratio characterizing the coupling strength, given by $U/t^x_\parallel$, is approximately 6 to 9, typically indicative of the strong coupling regime. The strong coupling scenario is also supported by Ref. [30], which suggests that the double-occupied state accounts for only about 5% of the electronic states.

Experimental evidence also supports strong correlations in bilayer $La_3Ni_2O_7$ [2,5]. Optical conductivity measurements [2] indicate a reduction in the electron' kinetic energy, supporting the Mott physics scenario. High-resolution angular-resolved photoemission spectroscopy (ARPES) experiments at ambient pressure [5] reveal a nearly flat γ band situated approximately 50 meV below the Fermi level, predominantly composed of $3d_{z^2}$ orbital. The effective mass enhancement for the $3d_{z^2}$ and $3d_{x^2-y^2}$ orbitals are approximately 8 and 2, respectively, possibly relating to the electron correlation. These experimental observations are critical for understanding the strong, orbital-dependent correlations in $La_3Ni_2O_7$ and their role in the material's superconducting properties.

B. The bilayer t-J model

In the strong coupling limit, the Hubbard-U interaction generates an effective interlayer AFM spin superexchange $J_\perp$ for the $3d_{z^2}$ orbitals and an intralayer one $J_\parallel$ for the $3d_{x^2-y^2}$ orbitals, respectively. Two electrons in the same site but different E_g orbitals are aligned in their spin direction due to the strong Hund's coupling. Consequently, the interlayer superexchange $J_\perp$ of $3d_{z^2}$ orbital is transmitted to the $3d_{x^2-y^2}$ orbital [25]. Please note that this interlayer AFM coupling does not arise from the virtual hopping due to the interlayer tunneling between two $3d_{x^2-y^2}$ orbitals, which is negligible.

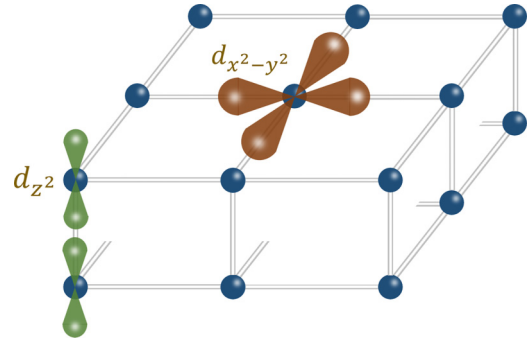

FIG. 1. Schematic figure of the bilayer E_g orbital model.

We arrive at an effective bilayer t-J two-orbital model as depicted in Fig. 1. The band part, or the t term, looks the same as Eq. (1) but under the constraint of no double-occupancy in each orbital. The interaction part reads

$$\begin{aligned} H_{J,x^2} =& J_\parallel \sum_{\langle i,j\rangle\alpha} \boldsymbol{S}_{x^2\alpha}(i) \cdot \boldsymbol{S}_{x^2\alpha}(j) \\ &+ J_\perp \sum_i \boldsymbol{S}_{x^2 1}(i) \cdot \boldsymbol{S}_{x^2 2}(i), \\ H_{J,z^2} =& J_\perp \sum_i \boldsymbol{S}_{z^2 1}(i) \cdot \boldsymbol{S}_{z^2 2}(i). \end{aligned} \tag{3}$$

The $3d_{x^2-y^2}$-orbital H_{J,x^2} takes the form of a bilayer t-$J_\parallel$-$J_\perp$ model [25,97]. Similar single-orbital bilayer t-$J_\parallel$-$J_\perp$ models have also been considered in the context of cuprates [63–71,97] and in cold atom systems [102–104]. For the $3d_{z^2}$-orbital H_{z^2}, only the interlayer superexchange $J_\perp$ is relevant.

The superexchange coupling parameters $J_\parallel$ and $J_\perp$ should in principle be determined by various interaction parameters in the strong-coupling limit [105], which is briefly summarized in Appendix A. For simplicity, we use the simple relation $J \approx 4t^2/U$ by neglecting other interaction parameters. Since the accurate value of the Hubbard U is hard to obtain, $J_\parallel$ and $J_\perp$ are set as tuning parameters. Since $J_\perp/J_\parallel \approx (t^z_\perp/t^x_\parallel)^2$, from the tight-binding parameters provided in Ref. [32] and Ref. [12], the ratio between two superexchange strengths is approximated as $J_\perp/J_\parallel \approx 1.7$–$1.8$. Similarly, $J_\perp/J_\parallel \approx 2$ as given in Ref. [21]. In our calculation, their values are tuned with their ratio fixed as $J_\perp/J_\parallel = 2$ for convenience. An estimation in Ref. [86] provides $U = 4.75$ eV, leading to $J_\parallel \approx 0.23$ eV. On the other hand, a smaller value of $J_\parallel = 0.1$ eV is used Ref. [21]. Considering the different values of parameters in literature, $J_\parallel$ is varied from 0.1 to 0.3 eV in our calculation to cover these variations.

III. THE SLAVE-BOSON MEAN-FIELD THEORY AND BAND RENORMALIZATION

The slave-boson approach [98,101] is a widely accepted methodology for studying the unconventional superconducting mechanism in quasi-2D systems. It offers a clear physical picture with spinons and holons as fundamental degrees of freedom, providing insights into interaction-renormalized spinon bands and the conditions necessary for superconductivity. The emergence of superconductivity hinges upon the pairing of spinons and the condensation of holons. Moreover, the slave-boson method offers valuable insights into the phenomenon of the pseudogap phase, identifying it with the presence of paired spinons in the absence of long-range phase coherence. In the following, we will perform this approach to explore the two-orbital model.

A. The Slave-boson-mean-field (SBMF) Approach

In the slave-boson approach [98,101], the electron operators of two E_g orbitals are represented as $d^\dagger_{a\alpha\sigma}(i) = f^\dagger_{a\alpha\sigma}(i)b_{a\alpha}(i)$, where $f^\dagger_{a\alpha\sigma}(i)$ is the spinon creation operator and $b_{a\alpha}(i)$ is the holon annihilation operator for the two orbitals ($a = x^2, z^2$), respectively. The following no-double-occupancy constraint is imposed on each orbital at each site,

$$\sum_\sigma f^\dagger_{a\alpha\sigma}(i)f_{a\alpha\sigma}(i) + b^\dagger_{a\alpha}(i)b_{a\alpha}(i) = 1. \tag{4}$$

These constraints are imposed through Lagrange multipliers $\lambda_{a\alpha}(i)$ and in the mean-field (MF) theory, $\lambda_{a\alpha}(i) \equiv \lambda_a$ on average irrespective of the layer and site.

The total electron filling $x_{\rm tot}$ of the E_g orbital is determined from the material, which yields $x_{\rm tot} = 0.75$ for LNO. The NN hybridization causes the density fluctuation between two orbitals while keeps the total holon density $\delta_{\rm tot} = 2 - 2x_{\rm tot}$ in the E_g orbitals per Ni site fixed,

$$\frac{1}{N}\sum_{i\alpha}\left(b^\dagger_{x^2\alpha}(i)b_{x^2\alpha}(i) + b^\dagger_{z^2\alpha}(i)b_{z^2\alpha}(i)\right) = 2\delta_{\rm tot}. \tag{5}$$

For the case of undoped LNO, $\delta_{\rm tot} = 0.5$. Upon chemical doping, $\delta_{\rm tot}$ varies within $0 \sim 1$, and is controlled by $\lambda_{\rm tot}$. $\lambda_{\rm tot}$ plays the role of chemical potential. In addition to $\lambda_{\rm tot}$, λ_{x^2}, λ_{z^2} are also introduced. Their combinations together with the onsite Δ_g act as 4 chemical potentials for the four degrees of freedom, i.e., spinons and holons in two E_g orbitals, respectively.

After the decomposition, the nearest neighboring AFM superexchange $J_\parallel$ and $J_\perp$ terms give rise to spinon's intraorbital bondings and singlet pairings see Appendix B for the details. The $\chi^a_{\parallel\alpha}(i,j)$ ($\alpha = 1, 2$) and $\chi^a_\perp(i)$ represent spinon's intra and interlayer hopping, respectively. $\Delta^a_{\parallel\alpha}(i,j)$ and $\Delta^a_\perp(i)$ represent the intra- and interlayer singlet pairings, respectively. The electron hopping terms of $t^a_\parallel$ and $t^z_\perp$ are decoupled as the intraorbital spinon hopping $\chi^a_{\parallel\alpha}(i,j)$ and $\chi^z_\perp(i)$ as well as holon hopping $\kappa^a_{\parallel\alpha}(i,j)$ and $\kappa^z_\perp(i)$, respectively. The interorbital electron hybridization $t^{xz}_{\parallel,j-i}$ term is decoupled as the interorbital spinon hybridization $\chi^{xz}_{\parallel\alpha}(i,j)$ and holon hybridization $\kappa^{xz}_{\parallel\alpha}(i,j)$, respectively. The various parameters defined above are expressed in terms of the expectation values of the corresponding fermion bilinear operators at thermal equilibrium for finite temperature, or at ground state for zero temperature. At the mean-field level, order parameters are assumed to be site/layer independent. The spinon hopping parameters are expressed as

$$\begin{aligned}
\chi^a_\parallel &= \tfrac{3}{8}J_\parallel\langle f^\dagger_{a\alpha\uparrow}(j)f_{a\alpha\uparrow}(i) + f^\dagger_{a\alpha\downarrow}(j)f_{a\alpha\downarrow}(i)\rangle,\\
\chi^a_\perp &= \tfrac{3}{8}J_\perp\langle f^\dagger_{a2\uparrow}(i)f_{a1\uparrow}(i) + f^\dagger_{a2\downarrow}(i)f_{a1\downarrow}(i)\rangle,\\
\chi^{xz}_\parallel &= t^{xz}_\parallel\langle f^\dagger_{z^2\alpha\uparrow}(j)f_{x^2\alpha\uparrow}(i) + f^\dagger_{z^2\alpha\downarrow}(j)f_{x^2\alpha\downarrow}(i)\rangle,
\end{aligned} \tag{6}$$

respectively, where $\langle\cdots\rangle$ means the thermal average. Here, for intralayer hopping, only the hopping between nearest-neighbor sites i and j is considered. Similarly, this convention is also assumed in the following. The spinon pairing order parameters are expressed as

$$\begin{aligned}
\Delta^a_\parallel &= \tfrac{3}{8}J_\parallel\langle f_{a\alpha\downarrow}(j)f_{a\alpha\uparrow}(i) - f_{a\alpha\uparrow}(j)f_{a\alpha\downarrow}(i)\rangle,\\
\Delta^a_\perp &= \tfrac{3}{8}J_\perp\langle f_{a2\downarrow}(i)f_{a1\uparrow}(i) - f_{a2\uparrow}(i)f_{a1\downarrow}(i)\rangle,
\end{aligned} \tag{7}$$

respectively. Similarly for the holon part, their hopping parameters are defined as follows as

$$\begin{aligned}
\kappa^a_\parallel &= t^a_\parallel\langle b^\dagger_{a\alpha}(j)b_{a\alpha}(i)\rangle,\\
\kappa^a_\perp &= t^a_\perp\langle b^\dagger_{a2}(i)b_{a1}(i)\rangle,\\
\kappa^{xz}_\parallel &= t^{xz}_\parallel\langle b^\dagger_{x^2\alpha}(j)b_{z^2\alpha}(i)\rangle.
\end{aligned} \tag{8}$$

The resultant mean-field Hamiltonians are presented in Appendix B. In the numerical calculations, all the order parameters and the Lagrange multipliers are solved self-consistently. In the LNO system, the physical occupations of the $3d_{z^2}$ and $3d_{x^2-y^2}$ orbitals slightly deviate from half- and quarter-filling, respectively, caused by their hybridization. The filling fraction x_a is related to the corresponding holon density δ_a via

$$x_a = (1 - \delta_a)/2, \tag{9}$$

in each E_g orbital represented by a.

For a typical value of the intralayer superexchange $J_\parallel = 0.25$ eV, the ground-state order parameters at zero temperature are calculated as listed in Table I. The interlayer s-wave pairing is stronger than the intralayer one as expected from the larger interlayer superexchange. Note that the obtained

TABLE I. Table of the hopping and pairing order parameters (OPs) as well as the holon densities δ_{x^2} and δ_{z^2} calculated by the SBMF theory in the ground state (GS). The corresponding band and interaction parameter values are $t^x_\parallel = 0.526$ eV, $t^z_\parallel = 0.113$ eV, $t^z_\perp = 0.676$ eV, $t^{xz}_\parallel = 0.25$ eV, $\Delta_g = 0.528$ eV, $J_\parallel = 0.25$ eV, and $J_\perp/J_\parallel = 2$.

OP	GS value (eV)	OP	GS value (eV)
$\chi^x_\parallel$	3.1×10^{-2}	$\chi^z_\parallel$	-1.6×10^{-6}
$\chi^x_\perp$	4.2×10^{-4}	$\chi^z_\perp$	1.8×10^{-1}
$\Delta^x_\parallel$	2.2×10^{-5}	$\chi^{xz}_\parallel$	4.5×10^{-3}
$\Delta^x_\perp$	9.7×10^{-3}	$\Delta^z_\perp$	4.0×10^{-2}
$\kappa^x_\parallel$	2.5×10^{-1}	$\kappa^z_\parallel$	2.2×10^{-3}
$\kappa^{xz}_\parallel$	2.4×10^{-2}	$\kappa^z_\perp$	1.3×10^{-2}
	Holon density		Holon density
δ_{x^2}	4.8×10^{-1}	δ_{z^2}	2.0×10^{-2}

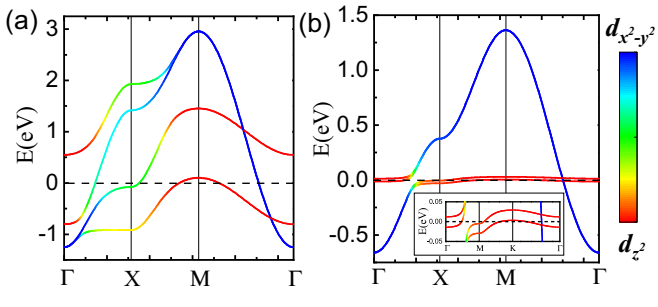

FIG. 2. (a) Tight-binding band structure and (b) the spinon band structure. The right-side color panel shows the orbital component with the red and blue colors representing the $3d_{z^2}$ and $3d_{x^2-y^2}$ orbitals, respectively. There exist four bands respecting two orbitals and bonding/antibonding hybridization. In the Mott limit, strong correlation effect flattens the $3d_{z^2}$ orbital dramatically and reduces the band splitting. The high symmetry points in the Brillouin zone are marked as $\Gamma(0,0)$, $X=(\pi,0)$, $M=(\pi,\pi)$. The inset in (b) shows zoom-in image of the spinon dispersion near Fermi level. (Note that the same band structure in (a) was first published in Ref. [39]. It is presented here for comparison).

$\delta_{z^2}=0.02$ suggests that the holon density in the $3d_{z^2}$ orbital is very low, which influences the electronic nature of the system as will be seen in the following sections.

B. Correlation induced band flattening

It is important to note that the band structure is significantly renormalized by strong electron correlation here. The tight-binding model yields the bare band structure as shown in Fig. 2(a), and in contrast the spinon band calculated in the SBMF theory is shown Fig. 2(b). The bare band structure shows four bands corresponding to two E_g orbitals and two layers, which are mixed together due to the interorbital hybridization and interlayer hopping. The lowest band is composed of the interlayer bonding state of the $3d_{z^2}$ orbital, mixed with $3d_{x^2-y^2}$ through hybridization. In contrast, the antibonding band of $3d_{z^2}$ is at high energy which can be neglected at low energy. The other two bands are dominated by the $3d_{x^2-y^2}$-orbital component. The above picture results in three Fermi surfaces: One is hole-like due to the bonding band of the $3d_{z^2}$ orbital, and the other two arise from $3d_{x^2-y^2}$.

As a comparison, in the spinon band shown in Fig. 2(b), both the $3d_{x^2-y^2}$-orbital bands and the $3d_{z^2}$ bands (the hybridized bands) are significantly flattened due to the constraint of no-double occupancy. The widths of the $3d_{x^2-y^2}$-orbital bands are reduced by a mild renormalization factor of $\delta_{x^2}\approx 0.5$. In contrast, the $3d_{z^2}$-band width (the hybridized bands) is much more strongly suppressed, renormalized by the factor of the holon densities $\sqrt{\delta_{x^2}\delta_{z^2}}\approx 0.1$ according to the holon densities calculated in Table I. Here, holon hybridization order parameter $\kappa_{\parallel}^{xz}$ is very small since the $3d_{z^2}$ orbital is nearly half filled with $\delta_{z^2}=0.02$. This result is qualitatively consistent with the recent ARPES experiment [5].

The ARPES detects the spectral function $A(\mathbf{k},\omega)$ of an electron below the Fermi level. For a free band fermion, $A(\mathbf{k},\omega)=\delta(\omega-\varepsilon_{\mathbf{k}})$, where $\varepsilon_{\mathbf{k}}$ indicates the band energy. For the t-J model, under the SBMF framework, the $A(\mathbf{k},\omega)$ becomes the convolution of the spectral functions of a spinon and a holon, respectively. Below the holon condensation temperature, $A(\mathbf{k},\omega)$ consists of a low-energy δ-peak of the spinon dispersion $\varepsilon_{\mathbf{k}}^{f}$ and a high-energy incoherent part. Above the holon condensation temperature, the δ peak is broadened, nevertheless, the spectral center remains approximately located at $\varepsilon_{\mathbf{k}}^{f}$. Note that in Fig. 2(b), only the interlayer bonding $3d_{z^2}$ spinon band and the lower half of the $3d_{x^2-y^2}$-spinon bands are physical, since the decomposition $c_{i\sigma}=f_{i\sigma}b_i^{\dagger}$ only stands when the spinon filling is less than $1/2$.

When holons are condensed, ARPES measures the spinon spectral function below the Fermi energy. Consequently, the ARPES observation (under ambient pressure) yields that the band width of $3d_{z^2-y^2}$ is flattened by a factor of about $1/2$, that of the $3d_{z^2}$ bonding band (the hybridized band) is flattened by a factor of about $\frac{1}{7}\sim\frac{1}{8}$ [5]. These observations are well consistent with our result. Note that although the ARPES experiment is carried out under ambient pressure, the strong correlation features remain.

IV. SUPERCONDUCTIVITY

There are two aspects regarding to the onset of superconductivity in each orbital, i.e., the gap formation and phase coherence. In the slave-boson approach, the gap formation is generated by the spinon pairing, and the phase coherence arises from the holon condensation [98,101]. Consequently, the superconducting order parameter is represented by the product between the spinon and holon parts,

$$\begin{aligned}\Delta_{\mathrm{SC}}^{a}&=\tfrac{3}{8}J\langle c_{a\alpha\downarrow}(j)c_{a\beta\uparrow}(i)-c_{a\alpha\uparrow}(j)c_{a\beta\downarrow}(i)\rangle\\&=\tfrac{3}{8}J\langle f_{a\alpha\downarrow}(j)f_{a\beta\uparrow}(i)-f_{a\alpha\uparrow}(j)f_{a\beta\downarrow}(i)\rangle\langle b_{a\alpha}^{\dagger}(j)b_{a\beta}^{\dagger}(i)\rangle.\end{aligned}\tag{10}$$

In the presence of holon condensation, each holon operator is simply replaced by a number as

$$b_{a\alpha}^{\dagger}(j)=b_{a\alpha}(i)\equiv\sqrt{\delta_a}.\tag{11}$$

Therefore the pairing symmetry is determined by the spinon part. The numerical results listed in Table I show an extended s-wave pairing for both orbitals. The interlayer pairing strength is much stronger than the intralayer one.

The driving force of this extended s-wave pairing is the strong interlayer superexchange interaction $J_{\perp}$ [25,97]. The superconducting T_c is determined by four temperature scales, including two spinon pairing temperatures T_{pair}^{x} and T_{pair}^{z}, and two holon condensation temperatures T_{BEC}^{x} and T_{BEC}^{z}. In two dimensions, the holon condensation temperature could be estimated from the Kosterlitz-Thouless (KT) transition point [106]. In the following, we shall first study the superconductivity in each orbital separately, and the coupling between them.

A. The $3d_{z^2}$ orbital induced SC

As shown in Table I, the ground-state value of $\Delta_{\perp}^{z}$ is largest among the pairing and hopping order parameters, which is brought by the strong interlayer superexchange $J_{\perp}$ and the flatness of the $3d_{z^2}$-orbital band (i.e., the hybridized band).

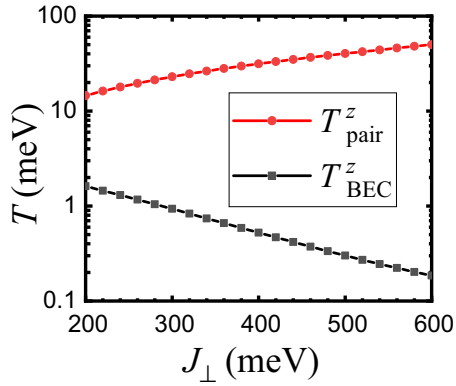

FIG. 3. Holon condensation temperature $T^z_{\rm BEC}$ and spinon pairing temperature $T^z_{\rm pair}$ vs interlayer superexchange $J_\perp$ for the $3d_{z^2}$ orbital. The on-set temperature of the $3d_{z^2}$ superconductivity is controlled by $T^z_{\rm BEC}$, which is much smaller. than $T^z_{\rm pair}$.

Consequently, the $3d_{z^2}$ orbital spinons start to pair at a high-temperature $T^z_{\rm pair}$ as shown in Fig. 3.

However, to reach superconductivity in the $3d_{z^2}$ orbital, the $3d_{z^2}$ holons need to condense. In 2D, the holon BEC is viewed as the KT transition which requires a finite holon density and the in-plane coherence. If without the orbital hybridization, the $3d_{z^2}$ orbital is exactly half-filled and there is no condensation. Taking into account hybridization, the $3d_{z^2}$ orbital acquires a finite hole doping transferred from $3d_{x^2-y^2}$. Moreover, the original localized $3d_{z^2}$ orbital acquires a narrow band width. Our numerical results displayed in Table I verify this scenario.

The holon Hamiltonian is presented in Eq. (B1) in Appendix B. Treating the hybridization term $H^{(b)}_{xz}$ as a perturbation, we investigate how it affects the in-plane hopping of the $3d_{z^2}$ holon. This can be done by directly diagonalizing the Hamiltonian Eq. (B1), and extracting the band dispersion. Consequently, the effective holon Hamiltonian for the $3d_{z^2}$ orbital is given by

$$\tilde{H}^{(b)}_{z^2} = \sum_{k\alpha} \tilde{\omega}_{z^2}(\boldsymbol{k}) b^\dagger_{z^2\alpha\boldsymbol{k}} b_{z^2\alpha\boldsymbol{k}} = \sum_{i,j,\alpha} \tilde{t}_{j-i} b^\dagger_{z^2\alpha}(i) b_{z^2\alpha}(j), \tag{12}$$

where $\tilde{\omega}_{z^2}(\boldsymbol{k})$ is the renormalized holon dispersion and $\tilde{t}_{j-i}$ reflects the effective in-plane hopping integral between the i and j sites. For a large distance l, the effective in-plane hopping integral decays promptly. In the numerical simulation, we only take the four nearest distances, as summarized in Table II. The displayed effective in-plane hopping integrals in Table II ($\sim$0.1 meV) are much smaller compared to the typical bare hopping integral of the system [$t^z_\parallel, t^{xz}_\parallel \sim \mathcal{O}(0.1)$ eV]. The reason for this result lies in the following.

The effective in-plane hopping of the $3d_{z^2}$-orbital holons arises from the direct NN hopping and the indirect process intermediated by the hybridization with the $3d_{x^2-y^2}$ orbital. The bare hopping integrals of these two process are not so small: $t^z_\parallel = 0.113$ eV and $t^{xz}_\parallel = 0.25$ eV. Nonetheless, under the no-double-occupancy constraint the in-plane holon hopping integrals should be renormalized by the spinon order

TABLE II. Effective hopping integrals $\tilde{t}_l$ for the $3d_{z^2}$-orbital holon at $J_\perp/J_\parallel = 2$, $J_\perp = 0.5$ eV without doping.

Direction vector $\vec{l}$	Distance l	Hopping integral $\tilde{t}_{\vec{l}}$ (meV)
(1,0)	1	0.167
(1,1)	$\sqrt{2}$	0.726
(2,0)	2	0.580
(2,1)	$\sqrt{5}$	0.212

parameters $\chi^z_\parallel$ and $\chi^{xz}_\parallel$ for the direct hopping and hybridization respectively, as shown in Eq. (B1). These renormalization factors are reversely determined by the spinon Hamiltonian (B2) in Appendix B. Due to the low holon density of the $3d_{z^2}$ orbital, its effective NN hopping strength $\chi^z_\parallel = -1.6 \times 10^{-3}$ meV is extremely small.

On the contrary, the spinon hybridization order parameter $\chi^{xz}_\parallel = 4.5$ meV is not very small. However, the hybridization-intermediated effective hopping for the $3d_{z^2}$ holons is only a second-order perturbative process, which leads to an effective hopping integral roughly estimated as $\tilde{t} \sim (\chi^{xz}_\parallel)^2/1$ eV $\sim$ 0.1 meV. This accounts for the small effective hopping integrals in Table II.

The effective holon model Eq. (12) undergoes KT transition due to phase fluctuations. Under the replacement, $b^\dagger_{z^2\alpha}(i) = \sqrt{\delta_{z^2}} e^{i\theta_{z^2\alpha}(i)}$, the system reduces to a generalized 2D XY-like model with interactions determined by the effective hopping integrals $\tilde{t}_{j-i}$. The superfluid stiffness $\rho_{z^2\alpha}$ could be further estimated from $\tilde{t}_{j-i}$,

$$\rho_{z^2\alpha} = 2\delta_{z^2} \sum_{\vec{l}} \tilde{t}_{\vec{l}}\, l^2, \tag{13}$$

where the summation takes over the bond directions $\vec{l}$. The KT transition temperature is proportional to the superfluid stiffness, $T^z_{\rm BEC} = \frac{\pi}{2}\rho_{z^2\alpha}$ [106].

The simulated pairing temperature $T^z_{\rm pair}$ and phase coherence temperature $T^z_{\rm BEC}$ as function of $J_\perp$ are displayed in Fig. 3. For the $3d_{z^2}$ orbital, $T^z_{\rm pair}$ is larger than $T^z_{\rm BEC}$ in several orders of magnitude. The SC of $3d_{z^2}$ orbital is determined by the coherence temperature $T^z_{\rm BEC}$. As $J_\perp = 2J_\parallel$ increases, the interlayer pairing of the $3d_{z^2}$ orbital is enhanced simultaneously, leading to a stronger $T^z_{\rm pair}$. On the contrary, the small $T^z_{\rm BEC}$ originates from the lack of holon density δ_{z^2} near half filling as well as the perturbative generation of the hopping integrals $\tilde{t}$, both of which are very small. As a result, the $T^z_{\rm BEC}$ for realistic $J_\perp$ is much lower than the experimental $T_c \approx 80$ K in LNO [1]. The experimental observed high superconducting T_c may not be caused by the $3d_{z^2}$ orbital due to the low $T^z_{\rm BEC}$.

B. The $3d_{x^2-y^2}$ orbital induced SC

The SC in the $3d_{x^2-y^2}$ orbital is analyzed by the same approach. Previously, we have derived an effective single $3d_{x^2-y^2}$-orbital bilayer t-J model by integrating out the $3d_{z^2}$-orbital spin degree of freedom [25], in which the J term is just represented by the H_{x^2} part of Hamiltonian in Eq. (3). For the $3d_{x^2-y^2}$ orbital, the hybridization term in Eq. (1) is only a perturbation, which does not obviously affect T_c. Therefore

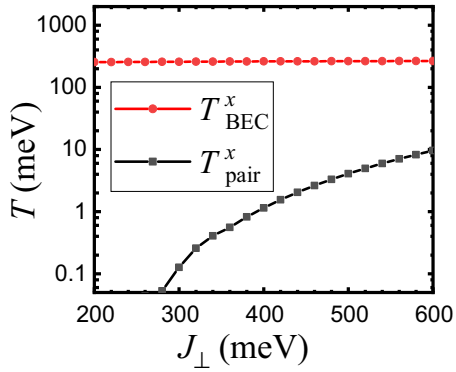

FIG. 4. Holon condensation temperature $T^x_{\rm BEC}$ and spinon pairing temperature $T^x_{\rm pair}$ vs interlayer superexchange $J_\perp$ for the $3d_{x^2}$ orbital.

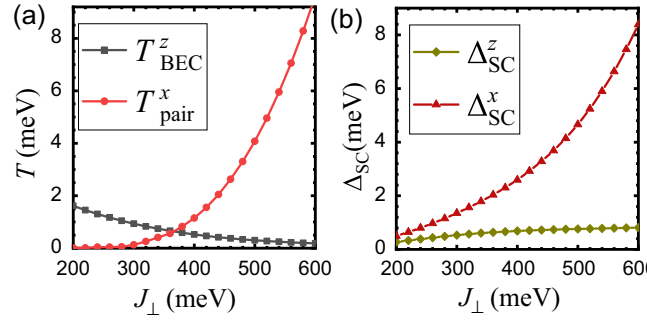

FIG. 5. (a). Superconducting temperature $T^z_{\rm BEC}$ and $T^x_{\rm pair}$ for the two orbitals. As $J_\perp$ becomes stronger, $T^z_{\rm BEC}$ decreases and $T^x_{\rm pair}$ increases. The superconducting nature will reverse at a critical strength. (b). Interlayer superconducting order parameters $\Delta^z_{\rm SC}$ and $\Delta^x_{\rm SC}$ as $J_\perp$ varies.

this term is first neglected in this section, and then will be investigated in detail in next section.

The condensation temperature of the $3d_{x^2-y^2}$-orbital holons $T^x_{\rm BEC}$ shown in Fig. 4 is very high (≈200 meV ≈2000 K), which serves as the largest temperature scale among the four temperatures relevant to the SC. Why $T^x_{\rm BEC}$ is so high is due to the following two aspects: the high holon density, i.e., 0.5, and the large in-plane hopping integral of the $3d_{x^2-y^2}$-orbital. This sets up the coherence condition for the $3d_{x^2-y^2}$-orbital to exhibit high-T_c superconductivity.

The pairing temperature of the $3d_{x^2-y^2}$-orbital spinons $T^x_{\rm pair}$ shown in Fig. 4 arises promptly with the enhancement of $J_\perp$ for fixed $J_\perp/J_\parallel = 2$. As clarified in our previous work reported in Ref. [25], the high $T^x_{\rm pair}$ originates from the strong interlayer superexchange interaction $J_\perp$, which drives the interlayer s-wave pairing symmetry in the system. As Fig. 4 shows $T^x_{\rm BEC} \gg T^x_{\rm pair}$, superconductivity in the $3d_{x^2-y^2}$ orbital degree of freedom is thus determined by its pairing temperature $T^x_{\rm pair}$.

C. SC in the two-orbital system

As clarified above, while the superconductivity in the $3d_{z^2}$ orbital is determined by its holon BEC temperature $T^z_{\rm BEC}$, that in the $3d_{x^2-y^2}$ orbital is determined by its spinon pairing temperature $T^x_{\rm pair}$. The dependence of these two temperature scales on $J_\perp$ is shown in Fig. 5(a) with the fixed value of $J_\perp/J_\parallel = 2$. It suggests that $T^z_{\rm BEC} > T^x_{\rm pair}$, or, $T^z_{\rm BEC} < T^x_{\rm pair}$, at weak or strong superexchange interaction, respectively. Since two orbitals are hybridized, when one orbital is superconducting, it induced superconductivity in the other via the proximity effect. Therefore the superconducting T_c in LNO is determined by the higher one between $T^z_{\rm BEC}$ and $T^x_{\rm pair}$.

In the realistic range of $J_\perp \in (200, 600)$ meV, Fig. 5(a) suggests that $T^z_{\rm BEC}$ is much lower than the experimental $T_c \approx$ 80 K. The low $T^z_{\rm BEC}$ originates from the no-double-occupancy constraint since the hybridization between two E_g orbitals is suppressed by strong correlations. Consequently, not only the holon density of the $3d_{z^2}$ orbital is very low, but also the effective in-plane holon hopping integrals are weak. The combination of these two aspects strongly suppresses the phase coherent temperature of the $3d_{z^2}$ orbitals and hence its superconducting T_c. What is more, as reported in Ref. [22], the Hund's rule coupling also strongly suppress the hybridization between the two E_g orbitals, which has not been considered here. Such an effect will further suppress the T_c of the $3d_{z^2}$ orbital. Therefore we conclude here that the $3d_{z^2}$ orbital is unlikely to play a dominant role in providing the superconducting mechanism in the LNO system.

The $3d_{x^2-y^2}$ orbital instead provides a possible mechanism to the high T_c in LNO comparable with experiment. Figure 5(a) suggests that the $T^x_{\rm pair}$ arises promptly with the enhancement of $J_\perp$, which can touch or even surpass the experimentally reported $T_c \approx 80$ K when $J_\parallel \in (0.25, 0.3)$ eV. Under the relation $J_\parallel = 4(t^x_\parallel)^2/U$, the estimated Hubbard $U =$ 4.75 eV [86] in combination with the provided $t^x_\parallel = 0.526$ eV yields $J_\parallel = 0.23$ eV, which is already very close to this regime. This result suggests that the $3d_{x^2-y^2}$ orbital plays a dominant role in the superconducting mechanism in the LNO system.

It is interesting to investigate the proximity effect between pairing gaps of two orbitals, which is induced by the H_{xz} term in Eq. (3) neglected in the last section. Table I suggests that the $3d_{z^2}$ orbital exhibits a large spinon pairing gap in the ground state, as verified in its large spinon pairing temperature $T^z_{\rm pair}$ shown in Fig. 3. This large $3d_{z^2}$-orbital spinon pairing gap considerably enhances the $3d_{x^2-y^2}$-orbital spinon pairing gap through the proximity effect induced by the hybridization between two orbitals since $\kappa^{xz}_\parallel$ is nonzero.

However, this can only happen below the condensation temperature $T^z_{\rm BEC}$ of the $3d_{z^2}$ orbital, under which SC is achieved in this orbital. This is because that, above $T^z_{\rm BEC}$, the phase fluctuation dictates $\langle b_{z^2i\alpha}\rangle = 0$ such that $\kappa^{xz}_\parallel = t^{xz}_\parallel \langle b^\dagger_{x^2i\alpha} b_{z^2i\alpha}\rangle = 0$. This analysis suggests that in Fig. 5(a), in the regime with $T^z_{\rm BEC} < T^x_{\rm pair}$, the proximity cannot happen when the temperature is near $T^x_{\rm pair}$, and thus T_c is set as $T_c = T^x_{\rm pair}$ which is blind to the H_{xz} term in Eq. (3). In contrast, in the regime with $T^z_{\rm BEC} > T^x_{\rm pair}$, the proximity effect directly drives superconductivity in the $3d_{x^2-y^2}$ orbital when $T < T^z_{\rm BEC}$. This analysis suggests that the physical T_c is determined by the higher one of $T^z_{\rm BEC}$ and $T^x_{\rm pair}$ shown in Fig. 5(a), which is not affected by the H_{xz} term in Eq. (3) in the SBMF framework.

Combining the spinon pairing and holon condensation together, we calculate the physical superconducting order

parameter expressed in the form of the c operator via Eq. (10). The ground-state interlayer-pairing superconducting order parameter of the two E_g orbitals as function of $J_\perp$ is shown in Fig. 5(b). Clearly, the ground-state superconducting order of the $3d_{x^2-y^2}$ orbital is stronger than that of the $3d_{z^2}$ orbital for all values of $J_\perp$ studied although the spinon gap of the former is much weaker than that of the latter, because the holon density in the $3d_{z^2}$ orbital is too low.

The above result is consistent with that obtained via the dynamic mean-field theory shown in Ref. [35]. It is interesting to note that in the regime wherein $T^z_{\rm BEC} > T^x_{\rm pair}$ so that the SC is induced by the $3d_{z^2}$ orbital, the ground-state superconducting order of the $3d_{x^2-y^2}$ orbital is still stronger than that of the $3d_{z^2}$ orbital, as the $3d_{x^2-y^2}$ spinon gap is considerably enhanced by the proximity effect in the ground state.

The viewpoint proposed here on why the high-T_c superconductivity in the LNO only emerges under pressure is different from that proposed in Ref. [1]. In the latter senario, the role of pressure is to lift upward the σ-bonding band consisting of the $3d_{z^2}$ orbital to cross the Fermi level and metallize it. Along this line, Refs. [30,34] further develop theories viewing $3d_{z^2}$ orbital as the driving force of superconductivity. In contrast, here we propose that the main role of pressure lies in that it enhances the interlayer coupling between the $3d_{z^2}$ orbitals to generate a strong interlayer superexchange interaction $J_\perp$, which is further transmitted to the $3d_{x^2-y^2}$ orbitals via the Hund's-rule coupling. After the $3d_{x^2-y^2}$ orbitals acquire the strong $J_\perp$, T_c is strongly enhanced in the entire system.

Of course, the metallization of the $3d_{z^2}$ band indirectly enhances the filling fraction of the $3d_{x^2-y^2}$ band through Eq. (5) and hence benefits its high T_c. However, the filling fraction of the $3d_{x^2-y^2}$ band can be enhanced by other approaches such as the chemical doping. As will be shown in the next section, the electron doping into LNO renders that the σ-bonding band is completely buried below the Fermi level, but the superconducting T_c enhances promptly. Therefore the metallization of the σ-bonding band is not necessary for the high-T_c SC in LNO.

V. DOPING EFFECT TO THE PHASE DIAGRAM

A. The chemical doping

Chemical doping serves as an important technique which may induce new physical phenomena. Here, we study the chemical doping into LNO to explore how superconductivity and pairing nature vary. At least, a possible hole-doping candidate is $La_{3-x}\,Sr_x\,Ni_2\,O_7$ ($x > 0$), whose electron number in the E_g orbitals per Ni atom becomes $1.5 - x/2$.

Let us consider by doping the LNO material, such that the total hole number per Ni atom in the E_g orbital is $\delta_{\rm tot}$. The derivation of its value from 0.5 means doping: $\delta_{\rm tot} < 0.5$ or $\delta_{\rm tot} > 0.5$ refers to electron-doping or hole-doping the LNO, respectively. Consequently, both the hole densities δ_s in the two orbitals ($s = x^2, z^2$) increases as increasing the total hole density $\delta_{\rm tot}$ as shown in Fig. 6(a). The holon condensation temperatures $T^s_{\rm BEC}$ and spinon pairing temperatures $T^s_{\rm pair}$ in the two orbitals versus $\delta_{\rm tot}$ are summarized in Fig. 6(b). The relations of the phase coherence and pairing temperatures in each orbital are similar to the undoped case, i.e., $\delta_{\rm tot} = 0.5$:

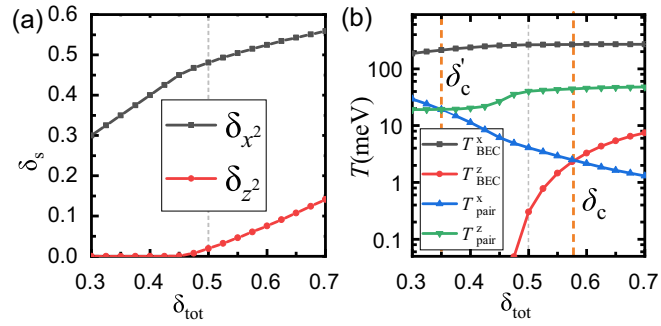

FIG. 6. (a). Realistic holon densities δ_{x^2} and δ_{z^2} vs total holon density $\delta_{\rm tot}$. (b). Doping dependence of the relevant four temperature scales for $J_\parallel = 0.25$ eV. Here, $T^z_{\rm BEC}$ and $T^x_{\rm pair}$ cross at a critical doping $\delta_c \approx 0.59$. $T^z_{\rm pair}$ and $T^x_{\rm pair}$ cross at another critical doping $\delta'_c \approx 0.35$.

$T^z_{\rm pair} \gg T^z_{\rm BEC}$ for the $3d_{z^2}$ orbital, and $T^x_{\rm BEC} \gg T^x_{\rm pair}$ for the $3d_{x^2-y^2}$ orbital. The physical superconducting T_c for the doped LNO is the higher of $T^z_{\rm BEC}$ and $T^x_{\rm pair}$.

We first consider the case of electron-doping in the regime $\delta_{\rm tot} < 0.5$. As shown in Fig. 6(b), $T^z_{\rm BEC}$ drops to zero promptly upon electron doping. The reason lies in that the hole density δ_{z^2} is suppressed to zero, and then phase coherence in the $3d_{z^2}$ orbital is lost. The situation for the $3d_{x^2-y^2}$ orbital is just on the contrary. As shown in Fig. 6(b), $T^x_{\rm pair}$ is quickly enhanced with electron doping, which reduces δ_{x^2} and enhances the density of state (DOS) of the $3d_{x^2-y^2}$ spinons. The similar situation occurs in cuprates: in the heavily overdoped regime, the reduction of doping significantly enhances T_c. For the physical T_c in LNO under electron doping, i.e.,$T_c = T^x_{\rm pair}$, is enhanced with electron doping.

The difference between our viewpoint and that held in Refs. [1,18,30,34] is more obvious in the electron-doped LNO. Consider the situation at $\delta_{\rm tot} = 0.35$. As shown in Fig. 7, tight-binding calculation yields that the σ-bonding band is completely buried below the Fermi surface. Then from the latter viewpoint, superconductivity is unfavorable. However, our result displayed in Fig. 6(b) suggests that the SC is not only maintained but also enhanced.

Now we come to the hole doping in the regime $\delta_{\rm tot} > 0.5$. Figure 6(b) suggests that upon the enhancement of hole doping, $T^z_{\rm BEC}$ grows promptly, while $T^x_{\rm pair}$ drops. The physical T_c is represents by the higher one between $T^z_{\rm BEC}$ and $T^x_{\rm pair}$, as

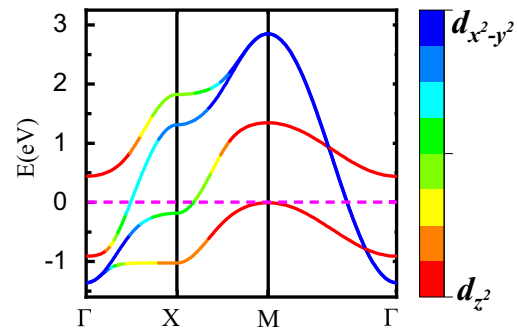

FIG. 7. Tight-binding band structure for the holon density $\delta_{\rm tot} = 0.35$. The dashed line indicates the Fermi level.

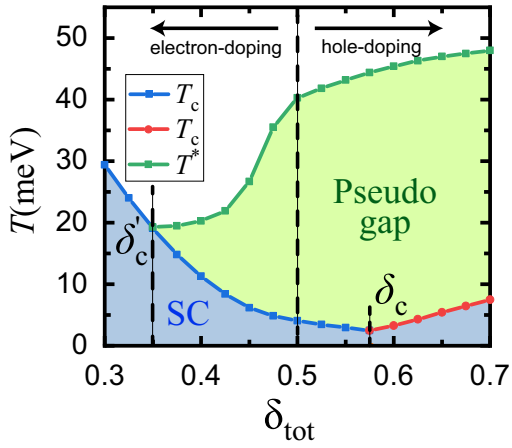

FIG. 8. Superconducting T_c and pseudogap temperature T^* vs δ_{tot}. $\delta_{tot} > 0.5$ corresponds to hole-doping while $\delta_{tot} < 0.5$ electron-doping. The upper curve (green line) determines the pseudogap phase from $3d_{z^2}$ orbital. The pseudogap phase merges into the superconducting phase at δ_c'. The lower curve determines the onset of superconductivity (SC), which has a local minima at δ_c.

depicted in Fig. 8. At the hole-doping level attains a critical one $\delta_c = 0.59$, the curves of $T^z_{\rm BEC}$ and $T^x_{\rm pair}$ cross. Thus, in the higher doping regime $\delta_{tot} > \delta_c$, T_c is represented by $3d_{z^2}$-holon condensation temperature, while in the lower doping regime $\delta_{tot} < \delta_c$, T_c is represented by $3d_{x^2-y^2}$-spinon pairing temperature. T_c shows non-monotonic behavior and has a minimum at $\delta_{tot} = \delta_c$.

It is interesting that on the two sides of the doping level δ_c, the nature of the superconducting transition is fundamentally different. Above δ_c, superconducting transition at $T_c = T^z_{\rm BEC}$ is driven by the $3d_{z^2}$ orbital and belongs to a BEC-type transition. On the contrary, below δ_c, the transition at $T_c = T^x_{\rm pair}$ is driven by the $3d_{x^2}$-orbital BCS-type transition. Such a change can be verified in such experiment as the optical conductivity: for the BEC transition driven by the kinetic energy, the onset of superconductivity is accompanied by a shift of the spectral weight from high to low frequencies; while for the BCS one, such phenomenon does not occur.

B. Pseudogap

The above two-orbital t-J model senario could also yield the pseudogap state in the high T_c LNO. The pseudogap takes place when spinons are paired while holons are uncondensed in the SBMF picture. Let us examine two relevant orbitals respectively. For the $3d_{x^2-y^2}$ orbital, since $T^x_{\rm BEC} \gg T^x_{\rm pair}$, i.e., the holon condensation temperature is much higher than the spinon pairing temperature, the pseudogap state should be absent in this channel. However, the situation is reversed in the $3d_{z^2}$ orbital since $T^z_{\rm BEC} \ll T^z_{\rm pair}$, and then $T^z_{\rm pair}$ behaves as the pseudogap temperature T^*. Of course, this requires $T^z_{\rm pair} > T_c$ which is satisfied unless in the extreme electron-doping regime. In particular, the pseduogap phase should appear in the undoped LNO, since $T_c = T^x_{\rm pair}$ and $T^* = T^z_{\rm pair}$ with $T_c \ll T^*$. The phase diagram based on the above analysis is shown in Fig. 8, including both the superconducting and pseudogap phases.

With the enhancement of hole doping, $T^* = T^z_{\rm pair}$ increases. Consequently, T^* is always higher than T_c, even though T_c can also rise when δ_{tot} is larger than δ_c. Therefore the hole-doping regime can host the pseudogap phase. With the enhancement of electron doping, T^* instead decreases due to the reduction of the DOS of the $3d_{z^2}$ spinons, as the Fermi level is lifting up toward the band top. Then $T_c = T^x_{\rm pair}$ on the contrary increases with electron doping due to the enhancement of the DOS of the $3d_{x^2-y^2}$ spinons. Consequently, the curves of T_c versus δ and T^* versus δ cross at another critical doping $\delta_c' \approx 0.35$.

Note that the pseudogap phenomenon here in LNO is significantly different from that in cuprates. In cuprates, the "optimal doping" divides the phase diagram into the underdoped and overdoped regimes, respectively. The optimal doping carries a two-fold role: It is where $T_c = T^*$, i.e., the pseudogap phase merges into the superconducting phase; and also where the superconductivity cross over from the BEC type to the BCS one. However, in LNO, the above two phenomena take place at different doping levels: δ_c marks the temperature the BEC and the BCS transition curves cross, and δ_c' marks where $T_c = T^*$. Furthermore, in LNO neither δ_c nor δ_c' marks the "optimal T_c", and δ_c actually marks a local minimum of T_c.

VI. DISCUSSION

In this study, high-T_c SC in $La_3Ni_2O_7$ under pressure is attributed primarily to the $3d_{x^2-y^2}$ orbital, whose holon condensation temperature is relatively high due to its large holon density [98,101]. As a result, holons condense at a relative high temperature. The $3d_{x^2-y^2}$-orbital SC is driven by the pairing of spinons, exhibiting BCS-like behavior. The formation of superconductivity is similar to the phenomena observed in overdoped cuprates [101].

The interlayer s-wave SC proposed in $La_3Ni_2O_7$ under pressure is distinct from the SC characteristics observed in other materials like cuprates [73,100,107,108]. For instance, Hg-based cuprates $HgBa_2CaCu_2O_{6+\delta}$ exhibit a bilayer structure, and T_c is enhanced compared to single-layer counterparts [108]. These bilayer cuprates typically feature an intralayer d-wave pairing symmetry of the $3d_{x^2-y^2}$ orbital, with only weak Josephson coupling between the layers. It has been suggested that the small contribution of $3d_{z^2}$ orbital near the Fermi level is important for its superconductivity [109]. In contrast, SC in bilayer nickelate $La_3Ni_2O_7$ is dominated by interbilayer s-wave pairing for the $3d_{x^2-y^2}$ orbital, driven by the strong interbilayer spin exchange.

Superconductivity has also been observed in doped infinite-layer nickelate $Nd_{0.8}Sr_{0.2}NiO_2$ [110], with hole doping into the Ni^{1+} $3d^9$ configuration. Orbital selective SC gaps have been proposed in the weak-coupling theory: a 2D $d_{x^2-y^2}$ pairing symmetry for the Ni $3d_{z^2-y^2}$-orbital and a 3D d_{z^2} pairing symmetry for the axial orbital composed of Nd/La d, Ni $3d_{z^2}$, and Ni s orbitals [111]. Reducing to the 2D case, the k_z quantum number disappears, and the d_{z^2} symmetry naturally evolves into an extended s-wave pairing, which is distinct from the interbilayer s-wave pairing proposed for bilayer $La_3Ni_2O_7$.

The present theory shares similarities with mixed valence systems, yet with characteristic differences. In mixed

valence compounds, additional pairing channels arise due to valence fluctuations mediated by emergent boson fields. Specifically, in a slave-boson treatment, valence fluctuations is characterized by holon density fluctuation, which can introduce an attractive pairing channel that gives rise to s-wave pairing [112].

VII. CONCLUSION

In this paper, we perform SBMF analysis to explore the interplay between $3d_{z^2}$ and $d_{x^2-y^2}$ orbitals based on the bilayer two-orbital t-J model. Our results reveal that due to the no-double-occupancy constraint, the $3d_{x^2-y^2}$ band and the σ-bonding $3d_{z^2}$ band are flattened by the factor 2 and 10 respectively, which is consistent with the ARPES observation [10]. Interlayer s-wave superconducting pairings within the two E_g orbitals dominate in the LNO material. For $3d_{z^2}$ orbital, its spinon pairing temperature T^z_{pair} is high and its holon condensation temperature T^z_{BEC} is very low since the no-double-occupancy constraint strongly suppresses the hybridization between the two E_g orbitals. The superconductivity induced by $3d_{z^2}$ orbital can hardly attain the experimental high T_c. Instead, the high-T_c superconductivity in LNO is induced by the $3d_{x^2-y^2}$ orbital, whose spinon pairing temperature T^x_{pair} is driven by the strong interlayer superexchange.

We have also studied the chemical doping effect to the LNO and obtain the phase diagram. Under electron doping, $T_c = T^x_{\text{pair}}$ continues to increase due to enhancement of the $3d_{x^2-y^2}$-spinons' DOS, although the σ-bonding $3d_{z^2}$ band is diving below the FS, suggesting that the metallization of this band is not necessary for the high-T_c SC in LNO. Under hole doping, $T_c = T^x_{\text{pair}}$ initially drops, and above a critical holon density $\delta_c = 0.59$ we have $T_c = T^z_{\text{BEC}}$, which begins to rise. Across the doping δ_c, the nature of the superconducting transition changes from the BCS type to the BEC type. Above the superconducting T_c, there exists an extra temperature scale T^*, i.e., the pseudogap temperature, which is given by the spinon pairing temperature of $3d_{z^2}$ orbital. The T^* enhances under hole doping and reduces under electron doping. The pseudogap phase merges into the superconducting phase below the holon density $\delta_c' = 0.35$. This interesting (T, δ) phase diagram calls for further experimental verification.

Finally, it is important to address certain limitations inherent in the effective model and slave-boson approach utilized in this study. While the slave-boson approach offers a direct insight and captures the essential physics of superconductivity and pseudogap phase, its practical applicability is constrained by several factors. For example, the mean-field approximation employed in this approach overlooks spatial modulation effects. The constraint of no double occupancy under large Hubbard U is only enforced on average in practice, disregarding the gauge fluctuations [101]. It is essential to acknowledge that the primary objective of this research is to offer a preliminary understanding to the observed high-T_c superconductivity in pressurized $La_3Ni_2O_7$, taking into both E_g orbitals. Further theoretical and experimental efforts are necessary to fully address and elucidate this phenomenon.

ACKNOWLEDGMENTS

We are grateful to the stimulating discussions with Wei Li, Yi-Zhuang You, Wei-Qiang Chen and Meng Wang. C.W. is supported by the National Natural Science Foundation of China under the Grants No. 12234016 and No. 12174317. F.Y. is supported by the National Natural Science Foundation of China under the Grants No. 12074031, and No. 11674025. C.L. is supported by the National Natural Science Foundation of China under the Grants No. 12304180. This work has been supported by the New Cornerstone Science Foundation.

APPENDIX A: EFFECTIVE TWO-ORBITAL MODEL

In this Appendix, we perform a detailed route to the effective t-$J_\perp$-$J_\parallel$ model from the two E_g orbitals Hubbard model Eqs. (1) and (2) with Hund's coupling J_H. In the bilayer nickelate $La_3Ni_2O_7$, $3d_{z^2}$ orbital is nearly half-filled while $3d_{x^2-y^2}$ orbital is roughly quarter-filled. AFM spin exchanges are generated in the strong Hubbard U limit. For simplicity, we could consider $U \gg 0$ limit and perform the conventional second perturbation theory. Consequently, in the strong coupling limit, we arrive at an effective t-J-J_H model described by the interaction

$$H_{J-J_H} = -J_H \sum_{i\alpha} \boldsymbol{S}_{z^2\alpha}(i)\cdot\boldsymbol{S}_{x^2\alpha}(i) + J_\parallel \sum_{\langle i,j\rangle\alpha} \boldsymbol{S}_{x^2\alpha}(i)\cdot\boldsymbol{S}_{x^2\alpha}(j) + J_\perp \sum_i \boldsymbol{S}_{z^21}(i)\cdot\boldsymbol{S}_{z^22}(i),$$

where the effective AFM interactions are roughly given by

$$J_\perp \approx \frac{4(t^z_\perp)^2}{U}, \qquad J_\parallel \approx \frac{4(t^x_\parallel)^2}{U}.$$

It should be noticed that a comprehensive analysis of the multiorbital model taken into account the Hund's rule would involve on-site interorbital spin-singlet and spin-triplet states.

To taken into account the effect of strong Hund's coupling, we can consider a pair of two sites labeled by 1 and 2 along a rung, with four spins locating at the two sites. The spin exchanges among the two orbitals in this rung is described by

$$H_{\text{rung}} = -J_H \boldsymbol{S}_{z^21}(i)\cdot\boldsymbol{S}_{x^21} - J_H \boldsymbol{S}_{z^22}\cdot\boldsymbol{S}_{x^22} + J_\perp \boldsymbol{S}_{z^21}\cdot\boldsymbol{S}_{z^22}.$$

In the strong Hund's limit $J_H \to +\infty$, the spins of the two E_g orbitals tend to form a spin triplet $\boldsymbol{S}_\alpha = \boldsymbol{S}_{z^2\alpha} + \boldsymbol{S}_{x^2\alpha}$ $(\alpha = 1, 2)$ with total spin $S_\alpha = 1$. As a result, the low-energy physics is described by an effective AFM spin exchange $\tilde{J}_\perp$ for the two spin-1 operators,

$$H^{\text{eff}}_{\text{rung}} = \tilde{J}_\perp \boldsymbol{S}_1\cdot\boldsymbol{S}_2 \to H^{\text{eff}\prime}_{\text{rung}} = \tilde{J}_\perp\left(\boldsymbol{S}_{x^21} + \boldsymbol{S}_{z^21}\right)\cdot\left(\boldsymbol{S}_{x^22} + \boldsymbol{S}_{z^22}\right).$$

The two Hamiltonians, $H^{\text{eff}}_{\text{rung}}$ and $H^{\text{eff}\prime}_{\text{rung}}$, describe the same low-energy physics: The ground state and the first excitation are total spin-0 and total spin-1 states respectively, constructing by two on site spin triplets. Focusing on the low-energy physics under strong coupling $\tilde{J}_\perp$, $H^{\text{eff}}_{\text{rung}}$ can be simplified into $H^{\text{eff}\prime}_{\text{rung}}$, within the on site spin triplet constraint be relaxed.

Due to the Hund's rule, the two on site spins of two orbitals are strongly aligned. The intraorbital spin exchanges

among $3d_{z^2}$ spins will generate intraorbital spin exchanges among $3d_{x^2}$ spins as well as interobrital spin exchanges under strong Hund's coupling. The exchanges of spin fluctuations could drive the spinon pairing. However, for the interorbital exchanges, the mismatch of the Fermi surface between the two orbitals naturally reduces the pairing tendency. Focusing on the superconductivity, only the effective intraobrital spin exchanges are important and the interorbital exchanges could be effectively omitted. It should also be remained that such interorbtial contribution could also effectively enhance the intraobrital exchagnes under the strong Hund's coupling, indirectly enhancing the intraorbital pairings.

APPENDIX B: SLAVE-BOSON MEAN-FIELD THEORY

In this Appendix, we perform the details of the slave-boson mean-field theory in the maintext. For the interlayer spin superexchange, the decomposition into hopping and singlet pairing channels is given by

$$\begin{aligned} J_\perp \boldsymbol{S}_{ai1}\cdot\boldsymbol{S}_{ai2} = &\frac{8}{3J_\perp}[|\chi^a_\perp(i)|^2+|\Delta^a_\perp(i)|^2]-[\chi^a_\perp(i)(f^\dagger_{a1\uparrow}(i)f_{a2\uparrow}(i)+f^\dagger_{a1\downarrow}(i)f_{a2\downarrow}(i))+\text{H.c.}] \\ &-[\Delta^a_\perp(i)(f^\dagger_{a1\uparrow}(i)f^\dagger_{a2\downarrow}(i)-f^\dagger_{a1\downarrow}(i)f^\dagger_{a2\uparrow}(i))+\text{H.c.}], \end{aligned}$$

where the interlayer spinon hoppings and pairings are defined as

$$\begin{aligned} \chi^a_\perp(i) &= \frac{3J_\perp}{8}(f^\dagger_{a2\uparrow}(i)f_{a1\uparrow}(i)+f^\dagger_{a2\downarrow}(i)f_{a1\downarrow}(i))\to\chi^a_\perp, \\ \Delta^a_\perp(i) &= \frac{3J_\perp}{8}(f_{a2\downarrow}(i)f_{a1\uparrow}(i)-f_{a2\uparrow}(i)f_{a1\downarrow}(i))\to\Delta^a_\perp \end{aligned}$$

with $a=x^2,z^2$ for the two orbitals, respectively. Similar decomposition holds for the intralayer superexchange,

$$\begin{aligned} J_\parallel \boldsymbol{S}_{a\alpha}(i)\cdot\boldsymbol{S}_{a\alpha}(j) = &\frac{8}{3J_\parallel}\left[\left|\chi^a_{\parallel\alpha}(i,j)\right|^2+\left|\Delta^a_{\parallel\alpha}(i,j)\right|^2\right]-\left[\chi^a_{\parallel\alpha}(i,j)(f^\dagger_{a\alpha\uparrow}(i)f_{a\alpha\uparrow}(j)+f^\dagger_{a\alpha\downarrow}(i)f_{a\alpha\downarrow}(j))+\text{H.c.}\right] \\ &-\left[\Delta^a_{\parallel\alpha}(i,j)(f^\dagger_{a\alpha\uparrow}(i)f^\dagger_{a\alpha\downarrow}(j)-f^\dagger_{a\alpha\downarrow}(i)f^\dagger_{a\alpha\uparrow}(j))+\text{H.c.}\right], \end{aligned}$$

where the intralayer spinon hoppings and pairings are defined as

$$\begin{aligned} \chi^a_{\parallel\alpha}(i,j) &= \frac{3J_\parallel}{8}\left(f^\dagger_{a\alpha\uparrow}(j)f_{a\alpha\uparrow}(i)+f^\dagger_{a\alpha\downarrow}(j)f_{a\alpha\downarrow}(i)\right)\to\chi^a_\parallel, \\ \Delta^a_{\parallel\alpha}(i,j) &= \frac{3J_\parallel}{8}\left(f_{a\alpha\downarrow}(j)f_{a\alpha\uparrow}(i)-f_{a\alpha\uparrow}(j)f_{a\alpha\downarrow}(i)\right)\to\Delta^a_\parallel. \end{aligned}$$

The holon hoppings are defined as

$$\begin{aligned} \kappa^a_{\parallel\alpha}(i,j) &= t^a_\parallel b_{a\alpha}(i)b^\dagger_{a\alpha}(j)\to\kappa^a_\parallel, \\ \kappa^a_\perp(i) &= t^a_\perp b^\dagger_{a2}(i)b_{a1}(i)\to\kappa^a_\perp, \\ \kappa^{xz}_{\parallel\alpha}(i,j) &= t^{xz}_\parallel b^\dagger_{x^2\alpha}(j)b_{z^2\alpha}(i)\to\kappa^{xz}_\parallel. \end{aligned}$$

The hopping term can be directly decoupled, e.g.,

$$t^x_\parallel\sum_\sigma\left(d^\dagger_{x^2\alpha\sigma}(i)d_{x^2\alpha\sigma}(j)+\text{H.c.}\right)=\sum_\sigma\left(\kappa^{x^2}_{\parallel\alpha}(i,j)f^\dagger_{x^2\alpha\sigma}(i)f_{x^2j\alpha\sigma}(j)+\text{H.c.}\right)+\left(\frac{t^x_\parallel}{3J_\parallel/8}\chi^{x^2}_{\parallel\alpha}(i,j)b^\dagger_{x^2\alpha}(i)b_{x^2\alpha}(j)+\text{H.c.}\right)$$

and similar decomposition for the other hopping terms. Based on these decoupling formulation, we could obtain the mean-field Hamiltonian.

After the mean-field decomposition, we arrive at the resultant MF Hamiltonian. The holon part reads

$$\begin{aligned} H^{(b)}_{\text{MF}} = &-(\delta\mu+\mu_b)\sum_{i\alpha}b^\dagger_{x^2\alpha}(i)b_{x^2\alpha}(i)-\mu_b\sum_{i\alpha}b^\dagger_{z^2\alpha}(i)b_{z^2\alpha}(i) \\ &-\frac{t^z_\parallel}{3J_\parallel/8}\chi^x_\parallel\sum_{\langle i,j\rangle\alpha}\left(b^\dagger_{x^2\alpha}(i)b_{x^2\alpha}(j)+\text{H.c.}\right)-\frac{t^z_\parallel}{3J_\parallel/8}\chi^z_\parallel\sum_{\langle i,j\rangle\alpha}\left(b^\dagger_{z^2\alpha}(i)b_{z^2\alpha}(j)+\text{H.c.}\right) \\ &-\frac{t^z_\perp}{3J_\perp/8}\chi^z_\perp\sum_i\left(b^\dagger_{z^21}(i)b_{z^22}(i)+\text{H.c.}\right)-\chi^{xz}_\parallel\sum_{\langle i,j\rangle\alpha}\left(b^\dagger_{x^2\alpha}(i)b_{z^2\alpha}(j)+b^\dagger_{z^2\alpha}(i)b_{x^2\alpha}(j)+\text{H.c.}\right), \end{aligned} \tag{B1}$$

where the chemical potentials are given by, $\mu_b=\lambda_{z^2}+\lambda_{\text{tot}}$ for $3d_{z^2}$ orbital and $\mu_b+\delta\mu=\lambda_{x^2}+\lambda_{\text{tot}}$ for $3d_{x^2-y^2}$ orbital. They fix the total density constraint.

For the spinon part, the mean-field result is

$$
\begin{aligned}
H_{\mathrm{MF}}^{(f)} = {} & (\Delta_g - \delta\mu - \mu_f)\sum_{i\alpha\sigma} f^\dagger_{x^2\alpha\sigma}(i) f_{x^2 i\alpha\sigma}(i) - (\delta\mu + \mu_f)\sum_{i\alpha\sigma} f^\dagger_{z^2\alpha\sigma}(i) f_{z^2\alpha\sigma}(i) \\
& - (\kappa_\parallel^x + \chi_\parallel^x)\sum_{\langle i,j\rangle\alpha\sigma}\left(f^\dagger_{x^2\alpha\sigma}(i) f_{x^2\alpha\sigma}(j) + \mathrm{H.c.}\right) - \kappa_\parallel^z \sum_{\langle i,j\rangle\alpha\sigma}\left(f^\dagger_{z^2\alpha\sigma}(i) f_{z^2\alpha\sigma}(j) + \mathrm{H.c.}\right) \\
& - \kappa_\parallel^{xz}\sum_{i\alpha}\left(f^\dagger_{x^2\alpha\sigma}(i) f_{z^2\alpha\sigma}(i+x) + f^\dagger_{z^2\alpha\sigma}(i) f_{x^2\alpha\sigma}(i+x) - f^\dagger_{x^2\alpha\sigma}(i) f_{z^2\alpha\sigma}(i+y) - f^\dagger_{z^2\alpha\sigma}(i) f_{x^2\alpha\sigma}(i+y) + \mathrm{H.c.}\right) \\
& - \sum_{i\sigma}\left(\chi_\perp^x f^\dagger_{x^2 1\sigma}(i) f_{x^2 2\sigma}(i) + \chi_\perp^z f^\dagger_{z^2 1\sigma}(i) f_{z^2 2\sigma}(i) + \mathrm{H.c.}\right) - \sum_i\left[\Delta_\perp^x\left(f^\dagger_{x^2 1\uparrow}(i) f^\dagger_{x^2 2\downarrow}(i) - f^\dagger_{x^2 1\downarrow}(i) f^\dagger_{x^2 2\uparrow}(i)\right) + \mathrm{H.c.}\right] \\
& - \sum_i\left[\Delta_\perp^z\left(f^\dagger_{z^2 1\uparrow}(i) f^\dagger_{z^2 2\downarrow}(i) - f^\dagger_{z^2 1\downarrow}(i) f^\dagger_{z^2 2\uparrow}(i)\right) + \mathrm{H.c.}\right] - \sum_{\langle i,j\rangle\alpha}\left[\Delta_\parallel^x\left(f^\dagger_{x^2\alpha\uparrow}(i) f^\dagger_{x^2\alpha\downarrow}(j) - f^\dagger_{x^2\alpha\downarrow}(i) f^\dagger_{x^2\alpha\uparrow}(j)\right) + \mathrm{H.c.}\right] \qquad \text{(B2)}
\end{aligned}
$$

with the chemical potentials for the two orbitals $\mu_f = \lambda_{z^2}$, $\mu_f + \delta\mu = \lambda_{x^2} + \lambda_{\mathrm{tot}}$.

Under Fourier transformation, the mean-field Hamiltonian takes the following form:

$$
H_{\mathrm{MF}}^{(b)} = \sum_{\boldsymbol{k}} \psi_b^\dagger(\boldsymbol{k}) H_b(\boldsymbol{k}) \psi_b(\boldsymbol{k}), \quad H_{\mathrm{MF}}^{(f)} = \sum_{\boldsymbol{k}} \Psi_f^\dagger(\boldsymbol{k}) H_f(\boldsymbol{k}) \Psi_f(\boldsymbol{k}),
$$

with the holon field $\psi_b(\boldsymbol{k})$ and spinon Nambu field $\Psi_f(\boldsymbol{k})$ given by

$$
\begin{aligned}
\psi_b(\boldsymbol{k}) &= \left(b_{x^2 1}(\boldsymbol{k}) b_{x^2 2}(\boldsymbol{k}) b_{z^2 1}(\boldsymbol{k}) b_{z^2 2}(\boldsymbol{k})\right)^T, \\
\Psi_f(\boldsymbol{k}) &= \left(f_{x^2 1\uparrow}(\boldsymbol{k}) f_{x^2 2\uparrow}(\boldsymbol{k}) f_{z^2 1\uparrow}(\boldsymbol{k}) f_{z^2 2\uparrow}(\boldsymbol{k}) f^\dagger_{x^2 1\downarrow}(-\boldsymbol{k}) f^\dagger_{x^2 2\downarrow}(-\boldsymbol{k}) f^\dagger_{z^2 1\downarrow}(-\boldsymbol{k}) f^\dagger_{z^2 2\downarrow}(-\boldsymbol{k})\right)^T.
\end{aligned}
$$

The quadratic Hamiltonian $H_{\mathrm{MF}}^{f,b}$ can be diagonalized through unitary transformations,

$$
H_{\mathrm{MF}}^{(b)} = \sum_{\boldsymbol{k}} \tilde{\psi}^\dagger_{b\boldsymbol{k}} E_{\boldsymbol{k}}^{(b)} \tilde{\psi}_{b\boldsymbol{k}} + \cdots, \quad H_{\mathrm{MF}}^{(f)} = \sum_{\boldsymbol{k}} \gamma_{\boldsymbol{k}}^\dagger E_{\boldsymbol{k}}^{(f)} \gamma_{\boldsymbol{k}} + \cdots,
$$

where $E_{\boldsymbol{k}}^{(b)}$ and $E_{\boldsymbol{k}}^{(f)}$ are eigenvalue matrices for $H_b(\boldsymbol{k})$ and $H_f(\boldsymbol{k})$, respectively. $\tilde{\psi}_{b\boldsymbol{k}} = U_b^\dagger(\boldsymbol{k})\psi_b(\boldsymbol{k})$ and $\gamma_{\boldsymbol{k}} = U_f^\dagger(\boldsymbol{k})\Psi_f(\boldsymbol{k})$ are the quasi-particle creation operators for the holon field and spinon field, with unitary transformation matrices $U_{b,f}^\dagger(\boldsymbol{k})$ diagonalizing $H_{\mathrm{MF}}^{(b,f)}$, respectively. The mean-field self-consistent equations Eqs. (6)–(8) can be obtained based on these mean-field Hamiltonian $H_{\mathrm{MF}}^{(f)}$ and $H_{\mathrm{MF}}^{(b)}$. For the spinon hopping order parameters, we have

$$
\begin{aligned}
\chi_\parallel^a &= \frac{3}{8} J_\parallel \sum_{\boldsymbol{k}} \cos(\boldsymbol{k}\cdot\boldsymbol{\mu})\langle f^\dagger_{a\alpha\uparrow}(\boldsymbol{k}) f_{a\alpha\uparrow}(\boldsymbol{k}) + f^\dagger_{a\alpha\downarrow}(\boldsymbol{k}) f_{a\alpha\downarrow}(\boldsymbol{k})\rangle, \\
\chi_\perp^a &= \frac{3}{8} J_\perp \sum_{\boldsymbol{k}} \langle f^\dagger_{a2\uparrow}(\boldsymbol{k}) f_{a1\uparrow}(\boldsymbol{k}) + f^\dagger_{a2\downarrow}(\boldsymbol{k}) f_{a1\downarrow}(\boldsymbol{k})\rangle, \\
\chi_\parallel^{xz} &= t_\parallel^{xz} \sum_{\boldsymbol{k}} \cos(\boldsymbol{k}\cdot\boldsymbol{\mu})\left\langle f^\dagger_{z^2\alpha\uparrow}(\boldsymbol{k}) f_{x^2\alpha\uparrow}(\boldsymbol{k}) + f^\dagger_{z^2\alpha\downarrow}(\boldsymbol{k}) f_{x^2\alpha\downarrow}(\boldsymbol{k})\right\rangle,
\end{aligned}
$$

where $\langle\cdots\rangle$ means the thermal average based on the mean-field Hamiltonian $H_{\mathrm{MF}}^{(f)}$ and $\boldsymbol{\mu} = \hat{x}, \hat{y}$ represents the nearest-neighbor directions. The spinon pairing order parameters are expressed as

$$
\begin{aligned}
\Delta_\parallel^a &= \frac{3}{8} J_\parallel \sum_{\boldsymbol{k}} \cos(\boldsymbol{k}\cdot\boldsymbol{\mu})\langle f_{a\alpha\downarrow}(\boldsymbol{k}) f_{a\alpha\uparrow}(\boldsymbol{k}) + f_{a\alpha\downarrow}(\boldsymbol{k}) f_{a\alpha\uparrow}(\boldsymbol{k})\rangle, \\
\Delta_\perp^a &= \frac{3}{8} J_\perp \sum_{\boldsymbol{k}} \langle f_{a2\downarrow}(\boldsymbol{k}) f_{a1\uparrow}(\boldsymbol{k}) + f_{a1\downarrow}(\boldsymbol{k}) f_{a2\uparrow}(\boldsymbol{k})\rangle.
\end{aligned}
$$

For the holon part, their hopping parameters are defined as follows as

$$
\begin{aligned}
\kappa_\parallel^a &= t_\parallel^a \sum_{\boldsymbol{k}} \cos(\boldsymbol{k}\cdot\boldsymbol{\mu})\langle b^\dagger_{a\alpha}(\boldsymbol{k}) b_{a\alpha}(\boldsymbol{k})\rangle, \\
\kappa_\perp^a &= t_\perp^a \sum_{\boldsymbol{k}} \langle b^\dagger_{a2}(\boldsymbol{k}) b_{a1}(\boldsymbol{k})\rangle, \quad \kappa_\parallel^{xz} = t_\parallel^{xz} \sum_{\boldsymbol{k}} \cos(\boldsymbol{k}\cdot\boldsymbol{\mu})\left\langle b^\dagger_{x^2\alpha}(\boldsymbol{k}) b_{z^2\alpha}(\boldsymbol{k})\right\rangle.
\end{aligned}
$$

[1] H. Sun, M. Huo, X. Hu, J. Li, Z. Liu, Y. Han, L. Tang, Z. Mao, P. Yang, B. Wang, J. Cheng, D.-X. Yao, G.-M. Zhang, and M. Wang, Signatures of superconductivity near 80k in a nickelate under high pressure, Nature (London) **621**, 493 (2023).

[2] Z. Liu, M. Huo, J. Li, Q. Li, Y. Liu, Y. Dai, X. Zhou, J. Hao, Y. Lu, M. Wang, and H.-H. Wen, Electronic correlations and energy gap in the bilayer nickelate $La_3Ni_2O_7$, Nat. Commun. **15**, 7570 (2024).

[3] J. Hou, P.-T. Yang, Z.-Y. Liu, J.-Y. Li, P.-F. Shan, L. Ma, G. Wang, N.-N. Wang, H.-Z. Guo, J.-P. Sun, Y. Uwatoko, M. Wang, G.-M. Zhang, B.-S. Wang, and J.-G. Cheng, Emergence of high-temperature superconducting phase in pressurized $La_3Ni_2O_7$ crystals, Chin. Phys. Lett. **40**, 117302 (2023).

[4] Y. Zhang, D. Su, Y. Huang, Z. Shan, H. Sun, M. Huo, K. Ye, J. Zhang, Z. Yang, Y. Xu, Y. Su, R. Li, M. Smidman, M. Wang, L. Jiao, and H. Yuan, High-temperature superconductivity with zero-resistance and strange metal behavior in $La_3Ni_2O_{7-\delta}$, Nat. Phys. **20**, 1269 (2024).

[5] J. Yang, H. Sun, X. Hu, Y. Xie, T. Miao, H. Luo, H. Chen, B. Liang, W. Zhu, G. Qu *et al.*, Orbital-dependent electron correlation in double-layer nickelate $La_3Ni_2O_7$, Nat. Commun. **15**, 4373 (2024).

[6] M. Zhang, C. Pei, Q. Wang, Y. Zhao, C. Li, W. Cao, S. Zhu, J. Wu, and Y. Qi, Effects of pressure and doping on Ruddlesden-popper phases $La_{n+1}Ni_nO_{3n+1}$, J. Mater. Sci. Technol. **185**, 147 (2024).

[7] G. Wang, N. N. Wang, X. L. Shen, J. Hou, L. Ma, L. F. Shi, Z. A. Ren, Y. D. Gu, H. M. Ma, P. T. Yang, Z. Y. Liu, H. Z. Guo, J. P. Sun, G. M. Zhang, S. Calder, J.-Q. Yan, B. S. Wang, Y. Uwatoko, and J.-G. Cheng, Pressure-induced superconductivity in polycrystalline $La_3Ni_2O_7$, Phys. Rev. X **14**, 011040 (2024).

[8] G. Wang, N. Wang, Y. Wang, L. Shi, X. Shen, J. Hou, H. Ma, P. Yang, Z. Liu, H. Zhang, X. Dong, J. Sun, B. Wang, K. Jiang, J. Hu, Y. Uwatoko, and J. Cheng, Observation of high-temperature superconductivity in the high-pressure tetragonal phase of $La_2PrNi_2O_{7-\delta}$, arXiv:2311.08212.

[9] L. Wang, Y. Li, S. Xie, F. Liu, H. Sun, C. Huang, Y. Gao, T. Nakagawa, B. Fu, B. Dong, Z. Cao, R. Yu, S. I. Kawaguchi, H. Kadobayashi, M. Wang, C. Jin, H. kwang Mao, and H. Liu, Structure responsible for the superconducting state in $La_3Ni_2O_7$ at low temperature and high pressure conditions, arXiv:2311.09186.

[10] Y. Zhou, J. Guo, S. Cai, H. Sun, P. Wang, J. Zhao, J. Han, X. Chen, Y. Chen, Q. Wu, Y. Ding, T. Xiang, H. K. Mao, and L. Sun, Investigations of key issues on the reproducibility of high-Tc superconductivity emerging from compressed $La_3Ni_2O_7$, arXiv:2311.12361.

[11] T. Cui, S. Choi, T. Lin, C. Liu, G. Wang, N. Wang, S. Chen, H. Hong, D. Rong, Q. Wang, Q. Jin, J.-O. Wang, L. Gu, C. Ge, C. Wang, J. G. Cheng, Q. Zhang, L. Si, K. juan Jin, and E.-J. Guo, Strain mediated phase crossover in Ruddlesden popper nickelates, Commun. Mater. **5**, 32 (2024).

[12] Z. Luo, X. Hu, M. Wang, W. Wú, and D.-X. Yao, Bilayer two-orbital model of $La_3Ni_2O_7$ under pressure, Phys. Rev. Lett. **131**, 126001 (2023).

[13] Y. Zhang, L.-F. Lin, A. Moreo, and E. Dagotto, Electronic structure, dimer physics, orbital-selective behavior, and magnetic tendencies in the bilayer nickelate superconductor $La_3Ni_2O_7$ under pressure, Phys. Rev. B **108**, L180510 (2023).

[14] Q.-G. Yang, D. Wang, and Q.-H. Wang, Possible $S_{\pm}$-wave superconductivity in $La_3Ni_2O_7$, Phys. Rev. B **108**, L140505 (2023).

[15] F. Lechermann, J. Gondolf, S. Bötzel, and I. M. Eremin, Electronic correlations and superconducting instability in $La_3Ni_2O_7$ under high pressure, Phys. Rev. B **108**, L201121 (2023).

[16] H. Sakakibara, N. Kitamine, M. Ochi, and K. Kuroki, Possible high T_c superconductivity in $La_3Ni_2O_7$ under high pressure through manifestation of a nearly half-filled bilayer Hubbard model, Phys. Rev. Lett. **132**, 106002 (2024).

[17] Y. Gu, C. Le, Z. Yang, X. Wu, and J. Hu, Effective model and pairing tendency in bilayer Ni-based superconductor $La_3Ni_2O_7$, arXiv:2306.07275.

[18] Y. Shen, M. Qin, and G.-M. Zhang, Effective Bi-layer model Hamiltonian and density-matrix renormalization group study for the high-T_c superconductivity $La_3Ni_2O_7$ under high pressure, Chin. Phys. Lett. **40**, 127401 (2023).

[19] V. Christiansson, F. Petocchi, and P. Werner, Correlated electronic structure of $La_3Ni_2O_7$ under pressure, Phys. Rev. Lett. **131**, 206501 (2023).

[20] D. A. Shilenko and I. V. Leonov, Correlated electronic structure, orbital-selective behavior, and magnetic correlations in double-layer $La_3Ni_2O_7$ under pressure, Phys. Rev. B **108**, 125105 (2023).

[21] W. Wú, Z. Luo, D.-X. Yao, and M. Wang, Superexchange and charge transfer in the nickelate superconductor $La_3Ni_2O_7$ under pressure, Sci. China Phys. Mech. Astron. **67**, 117402 (2024).

[22] Y. Cao and Y.-F. Yang, Flat bands promoted by Hund's rule coupling in the candidate double-layer high-temperature superconductor $La_3Ni_2O_7$ under high pressure, Phys. Rev. B **109**, L081105 (2024).

[23] X. Chen, P. Jiang, J. Li, Z. Zhong, and Y. Lu, Critical charge and spin instabilities in superconducting $La_3Ni_2O_7$, arXiv:2307.07154.

[24] Y.-B. Liu, J.-W. Mei, F. Ye, W.-Q. Chen, and F. Yang, $s^{\pm}$-wave pairing and the destructive role of apical-oxygen deficiencies in $La_3Ni_2O_7$ under pressure, Phys. Rev. Lett. **131**, 236002 (2023).

[25] C. Lu, Z. Pan, F. Yang, and C. Wu, Interlayer-coupling-driven high-temperature superconductivity in $La_3Ni_2O_7$ under pressure, Phys. Rev. Lett. **132**, 146002 (2024).

[26] Y. Zhang, L.-F. Lin, A. Moreo, T. A. Maier, and E. Dagotto, Structural phase transition, $s_{\pm}$-wave pairing, and magnetic stripe order in bilayered superconductor $la_3Ni_2O_7$ under pressure, Nat. Commun. **15**, 2470 (2024).

[27] H. Oh and Y.-H. Zhang, Type-II t-J model and shared superexchange coupling from Hund's rule in superconducting $La_3Ni_2O_7$, Phys. Rev. B **108**, 174511 (2023).

[28] Z. Liao, L. Chen, G. Duan, Y. Wang, C. Liu, R. Yu, and Q. Si, Electron correlations and superconductivity in $La_3Ni_2O_7$ under pressure tuning, Phys. Rev. B **108**, 214522 (2023).

[29] X.-Z. Qu, D.-W. Qu, J. Chen, C. Wu, F. Yang, W. Li, and G. Su, Bilayer t-J-$J_{\perp}$ model and magnetically mediated pairing in the pressurized nickelate $La_3Ni_2O_7$, Phys. Rev. Lett. **132**, 036502 (2024).

[30] Y.-F. Yang, G.-M. Zhang, and F.-C. Zhang, Interlayer valence bonds and two-component theory for high-T_c superconductivity of $La_3Ni_2O_7$ under pressure, Phys. Rev. B **108**, L201108 (2023).

[31] K. Jiang, Z. Wang, and F.-C. Zhang, High temperature superconductivity in $La_3Ni_2O_7$, Chin. Phys. Lett. **41**, 017402 (2023).

[32] Y. Zhang, L.-F. Lin, A. Moreo, T. A. Maier, and E. Dagotto, Trends in electronic structures and $s_{\pm}$-wave pairing for the rare-earth series in bilayer nickelate superconductor $R_3Ni_2O_7$, Phys. Rev. B **108**, 165141 (2023).

[33] J. Huang, Z. D. Wang, and T. Zhou, Impurity and vortex states in the bilayer high-temperature superconductor $La_3Ni_2O_7$, Phys. Rev. B **108**, 174501 (2023).

[34] Q. Qin and Y.-F. Yang, High-T_c superconductivity by mobilizing local spin singlets and possible route to higher T_c in pressurized $La_3Ni_2O_7$, Phys. Rev. B **108**, L140504 (2023).

[35] Y.-H. Tian, Y. Chen, J.-M. Wang, R.-Q. He, and Z.-Y. Lu, Correlation effects and concomitant two-orbital $s_{\pm}$-wave superconductivity in $La_3Ni_2O_7$ under high pressure, Phys. Rev. B **109**, 165154 (2024).

[36] D.-C. Lu, M. Li, Z.-Y. Zeng, W. Hou, J. Wang, F. Yang, and Y.-Z. You, Superconductivity from doping symmetric mass generation insulators: Application to $La_3Ni_2O_7$ under pressure, arXiv:2308.11195.

[37] R. Jiang, J. Hou, Z. Fan, Z.-J. Lang, and W. Ku, Pressure driven fractionalization of ionic spins results in cupratelike high-T_c superconductivity in $La_3Ni_2O_7$, Phys. Rev. Lett. **132**, 126503 (2024).

[38] N. Kitamine, M. Ochi, and K. Kuroki, Theoretical designing of multiband nickelate and palladate superconductors with $d^{8+\delta}$ configuration, arXiv:2308.12750.

[39] Z. Luo, B. Lv, M. Wang, W. Wú, and D.-X. Yao, High-T_c superconductivity in $La_3Ni_2O_7$ based on the bilayer two-orbital t-J model, npj Quantum Mater. **9**, 61 (2024).

[40] J.-X. Zhang, H.-K. Zhang, Y.-Z. You, and Z.-Y. Weng, Strong pairing originated from an emergent $\mathbb{Z}_2$ Berry phase in $La_3Ni_2O_7$, arXiv:2309.05726.

[41] Z. Pan, C. Lu, F. Yang, and C. Wu, Effect of rare-earth element substitution in superconducting $R_3Ni_2O_7$ under pressure, Chinese Phys. Lett. **41**, 087401 (2024).

[42] H. Sakakibara, M. Ochi, H. Nagata, Y. Ueki, H. Sakurai, R. Matsumoto, K. Terashima, K. Hirose, H. Ohta, M. Kato, Y. Takano, and K. Kuroki, Theoretical analysis on the possibility of superconductivity in the trilayer Ruddlesden-popper nickelate $La_4Ni_3O_{10}$ under pressure and its experimental examination: Comparison with $La_3Ni_2O_7$, Phys. Rev. B **109**, 144511 (2024).

[43] H. Lange, L. Homeier, E. Demler, U. Schollwöck, A. Bohrdt, and F. Grusdt, Pairing dome from an emergent Feshbach resonance in a strongly repulsive bilayer model, Phys. Rev. B **110**, L081113 (2024).

[44] B. Geisler, J. J. Hamlin, G. R. Stewart, R. G. Hennig, and P. Hirschfeld, Structural transitions, octahedral rotations, and electronic properties of $A_3Ni_2O_7$ rare-earth nickelates under high pressure, npj Quantum Mater. **9**, 38 (2024).

[45] H. Yang, H. Oh, and Y.-H. Zhang, Strong pairing from doping-induced Feshbach resonance and second Fermi liquid through doping a bilayer spin-one Mott insulator: Application to $La_3Ni_2O_7$, arXiv:2309.15095.

[46] L. C. Rhodes and P. Wahl, Structural routes to stabilize superconducting $La_3Ni_2O_7$ at ambient pressure, Phys. Rev. Mater. **8**, 044801 (2024).

[47] H. Lange, L. Homeier, E. Demler, U. Schollwöck, F. Grusdt, and A. Bohrdt, Feshbach resonance in a strongly repulsive bilayer model: A possible scenario for bilayer nickelate superconductors, Phys. Rev. B **109**, 045127 (2024).

[48] H. LaBollita, V. Pardo, M. R. Norman, and A. S. Botana, Electronic structure and magnetic properties of $La_3Ni_2O_7$ under pressure, arXiv:2309.17279.

[49] U. Kumar, C. Melnick, and G. Kotliar, Softening of dd excitation in the resonant inelastic x-ray scattering spectra as a signature of Hund's coupling in nickelates, arXiv:2310.00983.

[50] T. Kaneko, H. Sakakibara, M. Ochi, and K. Kuroki, Pair correlations in the two-orbital Hubbard ladder: Implications for superconductivity in the bilayer nickelate $La_3Ni_2o_7$, Phys. Rev. B **109**, 045154 (2024).

[51] S. Ryee, N. Witt, and T. O. Wehling, Critical role of interlayer dimer correlations in the superconductivity of $La_3Ni_2O_7$, Phys. Rev. Lett. **133**, 096002 (2024).

[52] Y. Zhang, L.-F. Lin, A. Moreo, T. A. Maier, and E. Dagotto, Electronic structure, magnetic correlations, and superconducting pairing in the reduced Ruddlesden-popper bilayer $La_3Ni_2O_6$ under pressure: Different role of $d_{3z^2-r^2}$ orbital compared with $La_3Ni_2O_7$, Phys. Rev. B **109**, 045151 (2024).

[53] H. Schlömer, U. Schollwöck, F. Grusdt, and A. Bohrdt, Superconductivity in the pressurized nickelate $La_3Ni_2O_7$ in the vicinity of a BEC-BCS crossover, arXiv:2311.03349.

[54] J. Chen, F. Yang, and W. Li, Orbital-selective superconductivity in the pressurized bilayer nickelate $La_3Ni_2O_7$: An infinite projected entangled-pair state study, Phys. Rev. B **110**, L041111 (2024).

[55] H. Liu, C. Xia, S. Zhou, and H. Chen, Role of crystal-field-splitting and longe-range-hoppings on superconducting pairing symmetry of $La_3Ni_2O_7$, arXiv:2311.07316.

[56] Z. Ouyang, J.-M. Wang, J.-X. Wang, R.-Q. He, L. Huang, and Z.-Y. Lu, Hund electronic correlation in $La_3Ni_2O_7$ under high pressure, Phys. Rev. B **109**, 115114 (2024).

[57] X.-Z. Qu, D.-W. Qu, W. Li, and G. Su, Roles of Hund's rule and hybridization in the two-orbital model for high-T_c superconductivity in the bilayer nickelate, arXiv:2311.12769.

[58] X. Sui, X. Han, X. Chen, L. Qiao, X. Shao, and B. Huang, Electronic properties of nickelate superconductor $R_3Ni_2O_7$ with oxygen vacancies (R=La or Ce), Phys. Rev. B **109**, 205156 (2024).

[59] Y.-Y. Zheng and W. Wú, Superconductivity in the bilayer two-orbital Hubbard model, arXiv:2312.03605.

[60] M. Kakoi, T. Kaneko, H. Sakakibara, M. Ochi, and K. Kuroki, Pair correlations of the hybridized orbitals in a ladder model for the bilayer nickelate $La_3Ni_2O_7$, Phys. Rev. B **109**, L201124 (2024).

[61] G. Heier, K. Park, and S. Y. Savrasov, Competing d_{xy} and $s_{\pm}$ pairing symmetries in superconducting $La_3Ni_2O_7$: LDA + FLEX calculations, Phys. Rev. B **109**, 104508 (2024).

[62] J. G. Bednorz and K. A. Müller, Possible high T_c superconductivity in the Ba-La-Cu-O system, Z. Phys. B **64**, 189 (1986).

[63] M. U. Ubbens and P. A. Lee, Spin-gap formation in bilayer cuprates due to enhanced interlayer pairing, Phys. Rev. B **50**, 438 (1994).

[64] K. Kuboki and P. A. Lee, Energy gap structure in bilayer oxide superconductors, J. Phys. Soc. Jpn. **64**, 3179 (1995).

[65] J. Maly, D. Z. Liu, and K. Levin, Superconducting order parameter symmetry in multilayer cuprates, Phys. Rev. B **53**, 6786 (1996).

[66] A. Nazarenko and E. Dagotto, Hole dispersion and symmetry of the superconducting order parameter for underdoped CuO_2 bilayers and the three-dimensional antiferromagnets, Phys. Rev. B **54**, 13158 (1996).

[67] A. Medhi, S. Basu, and C. Kadolkar, Phase diagram for a t-J bilayer: Role of interlayer couplings, Eur. Phys. J. B **72**, 583 (2009).

[68] R. Eder, Y. Ohta, and S. Maekawa, Ground-state properties and dynamics of the bilayer t-J model, Phys. Rev. B **52**, 7708 (1995).

[69] M. Vojta and K. W. Becker, Doped bilayer antiferromagnets: Hole dynamics on both sides of a magnetic ordering transition, Phys. Rev. B **60**, 15201 (1999).

[70] H. Zhao and J. R. Engelbrecht, $t-J$ model for a bilayer: Coexisting superconductivity and planar-flux phases, Phys. Rev. B **71**, 054508 (2005).

[71] M. Zegrodnik and J. Spałek, Effect of interlayer processes on the superconducting state within the t-J-U model: Full Gutzwiller wave-function solution and relation to experiment, Phys. Rev. B **95**, 024507 (2017).

[72] S. Chakravarty, H.-Y. Kee, and K. Völker, An explanation for a universality of transition temperatures in families of copper oxide superconductors, Nature (London) **428**, 53 (2004).

[73] C. Chu, L. Deng, and B. Lv, Hole-doped cuprate high temperature superconductors, Physica C **514**, 290 (2015).

[74] X. Luo, H. Chen, Y. Li, Q. Gao, C. Yin, H. Yan, T. Miao, H. Luo, Y. Shu, Y. Chen, C. Lin, S. Zhang, Z. Wang, F. Zhang, F. Yang, Q. Peng, G. Liu, L. Zhao, Z. Xu, T. Xiang, and X. J. Zhou, Electronic origin of high superconducting critical temperature in trilayer cuprates, Nat. Phys. **19**, 1841 (2023).

[75] S. Taniguchi, T. Nishikawa, Y. Yasui, Y. Kobayashi, J. Takeda, S.-I. Shamoto, and M. Sato, Transport, magnetic and thermal properties of $La_3Ni_2O_{7-\delta}$, J. Phys. Soc. Jpn. **64**, 1644 (1995).

[76] D.-K. Seo, W. Liang, M.-H. Whangbo, Z. Zhang, and M. Greenblatt, Electronic band structure and madelung potential study of the nickelates La_2NiO_4, $La_3Ni_2O_7$, and $La_4Ni_3O_{10}$, Inorg. Chem. **35**, 6396 (1996).

[77] Y. Kobayashi, S. Taniguchi, M. Kasai, M. Sato, T. Nishioka, and M. Kontani, Transport and magnetic properties of $La_3Ni_2O_{7-\delta}$ and $La_4Ni_3O_{10-\delta}$, J. Phys. Soc. Jpn. **65**, 3978 (1996).

[78] M. Greenblatt, Ruddlesden-popper $Ln_{n+1}Ni_nO_{3n+1}$ nickelates: Structure and properties, Curr. Opin. Solid State Mater. Sci. **2**, 174 (1997).

[79] M. Greenblatt, Z. Zhang, and M. Whangbo, Electronic properties of $La_3Ni_2O_7$ and $Ln_4Ni_3O_{10}$, Ln= La, Pr and Nd, Synth. Met. **85**, 1451 (1997).

[80] C. D. Ling, D. N. Argyriou, G. Wu, and J. Neumeier, Neutron diffraction study of $La_3Ni_2O_7$: Structural relationships among $n = 1, 2$, and 3 phases $La_{n+1}Ni_nO_{3n+1}$, J. Solid State Chem. **152**, 517 (2000).

[81] G. Wu, J. J. Neumeier, and M. F. Hundley, Magnetic susceptibility, heat capacity, and pressure dependence of the electrical resistivity of $La_3Ni_2O_7$ and $La_4Ni_3O_{10}$, Phys. Rev. B **63**, 245120 (2001).

[82] T. Fukamachi, Y. Kobayashi, T. Miyashita, and M. Sato, ^{139}La NMR studies of layered perovskite systems $La_3Ni_2O_{7-\delta}$ and $La_4Ni_3O_{10}$, J. Phys. Chem. Solids **62**, 195 (2001).

[83] V. I. Voronin, I. F. Berger, V. A. Cherepanov, L. Y. Gavrilova, A. N. Petrov, A. I. Ancharov, B. Tolochko, and S. G. Nikitenko, Neutron diffraction, synchrotron radiation and exafs spectroscopy study of crystal structure peculiarities of the lanthanum nickelates $La_{n+1}Ni_nO_y$ ($n = 1, 2, 3$), Nucl. Instrum. Methods Phys. Res., Sect. A **470**, 202 (2001).

[84] D. O. Bannikov, A. P. Safronov, and V. A. Cherepanov, Thermochemical characteristics of $La_{n+1}Ni_nO_{3n+1}$ oxides, Thermochim. Acta **451**, 22 (2006).

[85] T. Hosoya, K. Igawa, Y. Takeuchi, K. Yoshida, T. Uryu, H. Hirabayashi, and H. Takahashi, Pressure studies on the electrical properties in $R_{2-x}Sr_xNi_{1-y}Cu_yO_{4+\delta}$ (R=La, Nd) and $La_3Ni_2O_{7+\delta}$, J. Phys.: Conf. Ser. **121**, 052013 (2008).

[86] V. Pardo and W. E. Pickett, Metal-insulator transition in layered nickelates $La_3Ni_2O_{7-\delta}$ ($\delta = 0.0, 0.5, 1$), Phys. Rev. B **83**, 245128 (2011).

[87] M. Nakata, D. Ogura, H. Usui, and K. Kuroki, Finite-energy spin fluctuations as a pairing glue in systems with coexisting electron and hole bands, Phys. Rev. B **95**, 214509 (2017).

[88] Y. Mochizuki, H. Akamatsu, Y. Kumagai, and F. Oba, Strain-engineered Peierls instability in layered perovskite $La_3Ni_2O_7$ from first principles, Phys. Rev. Mater. **2**, 125001 (2018).

[89] Z. Li, W. Guo, T. T. Zhang, J. H. Song, T. Y. Gao, Z. B. Gu, and Y. F. Nie, Epitaxial growth and electronic structure of Ruddlesden–popper nickelates ($La_{n+1}Ni_nO_{3n+1}$, $n = 1 - 5$), APL Mater. **8**, 091112 (2020).

[90] J. Song, D. Ning, B. Boukamp, J.-M. Bassat, and H. J. Bouwmeester, Structure, electrical conductivity and oxygen transport properties of Ruddlesden–popper phases $Ln_{n+1}Ni_nO_{3n+1}$ (Ln=La, Pr and Nd; $n = 1$, 2 and 3), J. Mater. Chem. A **8**, 22206 (2020).

[91] M. R. Barone, N. M. Dawley, H. P. Nair, B. H. Goodge, M. E. Holtz, A. Soukiassian, E. E. Fleck, K. Lee, Y. Jia, T. Heeg, R. Gatt, Y. Nie, D. A. Muller, L. F. Kourkoutis, and D. G. Schlom, Improved control of atomic layering in perovskite-related homologous series, APL Mater. **9**, 021118 (2021).

[92] Z. Liu, H. Sun, M. Huo, X. Ma, Y. Ji, E. Yi, L. Li, H. Liu, J. Yu, Z. Zhang, Z. Chen, F. Liang, H. Dong, H. Guo, D. Zhong, B. Shen, S. Li, and M. Wang, Evidence for charge and spin density waves in single crystals of $La_3Ni_2O_7$ and $La_3Ni_2O_6$, Sci. China Phys. Mech. Astron. **66**, 217411 (2023).

[93] R. T. Scalettar, J. W. Cannon, D. J. Scalapino, and R. L. Sugar, Magnetic and pairing correlations in coupled Hubbard planes, Phys. Rev. B **50**, 13419 (1994).

[94] S. S. Kancharla and S. Okamoto, Band insulator to Mott insulator transition in a bilayer Hubbard model, Phys. Rev. B **75**, 193103 (2007).

[95] T. A. Maier and D. J. Scalapino, Pair structure and the pairing interaction in a bilayer Hubbard model for unconventional superconductivity, Phys. Rev. B **84**, 180513(R) (2011).

[96] M. Gall, N. Wurz, J. Samland, C. F. Chan, and M. Köhl, Competing magnetic orders in a bilayer Hubbard model with ultracold atoms, Nature (London) **589**, 40 (2021).

[97] T. Ma, D. Wang, and C. Wu, Doping-driven antiferromagnetic insulator-superconductor transition: A quantum Monte Carlo study, Phys. Rev. B **106**, 054510 (2022).

[98] G. Kotliar and J. Liu, Superexchange mechanism and d-wave superconductivity, Phys. Rev. B **38**, 5142(R) (1988).

[99] B. Keimer, S. A. Kivelson, M. R. Norman, S. Uchida, and J. Zaanen, From quantum matter to high-temperature superconductivity in copper oxides, Nature (London) **518**, 179 (2015).

[100] C. Proust and L. Taillefer, The remarkable underlying ground states of cuprate superconductors, Annu. Rev. Condens. Matter Phys. **10**, 409 (2019).

[101] P. A. Lee, N. Nagaosa, and X.-G. Wen, Doping a Mott insulator: Physics of high-temperature superconductivity, Rev. Mod. Phys. **78**, 17 (2006).

[102] A. Bohrdt, L. Homeier, C. Reinmoser, E. Demler, and F. Grusdt, Exploration of doped quantum magnets with ultracold atoms, Ann. Phys. **435**, 168651 (2021).

[103] A. Bohrdt, L. Homeier, I. Bloch, E. Demler, and F. Grusdt, Strong pairing in mixed-dimensional bilayer antiferromagnetic Mott insulators, Nat. Phys. **18**, 651 (2022).

[104] S. Hirthe, T. Chalopin, D. Bourgund, P. Bojović, A. Bohrdt, E. Demler, F. Grusdt, I. Bloch, and T. A. Hilker, Magnetically mediated hole pairing in fermionic ladders of ultracold atoms, Nature (London) **613**, 463 (2023).

[105] A. Chiesa, S. Carretta, P. Santini, G. Amoretti, and E. Pavarini, Many-body models for molecular nanomagnets, Phys. Rev. Lett. **110**, 157204 (2013).

[106] J. Kosterlitz and D. Thouless, Ordering, metastability and phase transitions in two-dimensional systems, J. Phys. C: Solid State Phys. **6**, 1181 (1973).

[107] E. Pavarini, I. Dasgupta, T. Saha-Dasgupta, O. Jepsen, and O. K. Andersen, Band-structure trend in hole-doped cuprates and correlation with T_c max, Phys. Rev. Lett. **87**, 047003 (2001).

[108] A. Iyo, Y. Tanaka, H. Kito, Y. Kodama, P. M. Shirage, D. D. Shivagan, H. Matsuhata, K. Tokiwa, and T. Watanabe, T_c vs n Relationship for Multilayered High-T_c Superconductors, J. Phys. Soc. Jpn. **76**, 094711 (2007).

[109] H. Sakakibara, K. Suzuki, H. Usui, S. Miyao, I. Maruyama, K. Kusakabe, R. Arita, H. Aoki, and K. Kuroki, Orbital mixture effect on the Fermi-surface–T_c correlation in the cuprate superconductors: Bilayer vs. single layer, Phys. Rev. B **89**, 224505 (2014).

[110] D. Li, K. Lee, B. Y. Wang, M. Osada, S. Crossley, H. R. Lee, Y. Cui, Y. Hikita, and H. Y. Hwang, Superconductivity in an infinite-layer nickelate, Nature (London) **572**, 624 (2019).

[111] P. Adhikary, S. Bandyopadhyay, T. Das, I. Dasgupta, and T. Saha-Dasgupta, Orbital-selective superconductivity in a two-band model of infinite-layer nickelates, Phys. Rev. B **102**, 100501(R) (2020).

[112] P. Adhikary and T. Das, Novel attractive pairing interaction in strongly correlated superconductors, SciPost Phys. **7**, 078 (2019).